Cell

Prefrontal deep projection neurons enable cognitive flexibility via persistent feedback monitoring

Graphical abstract

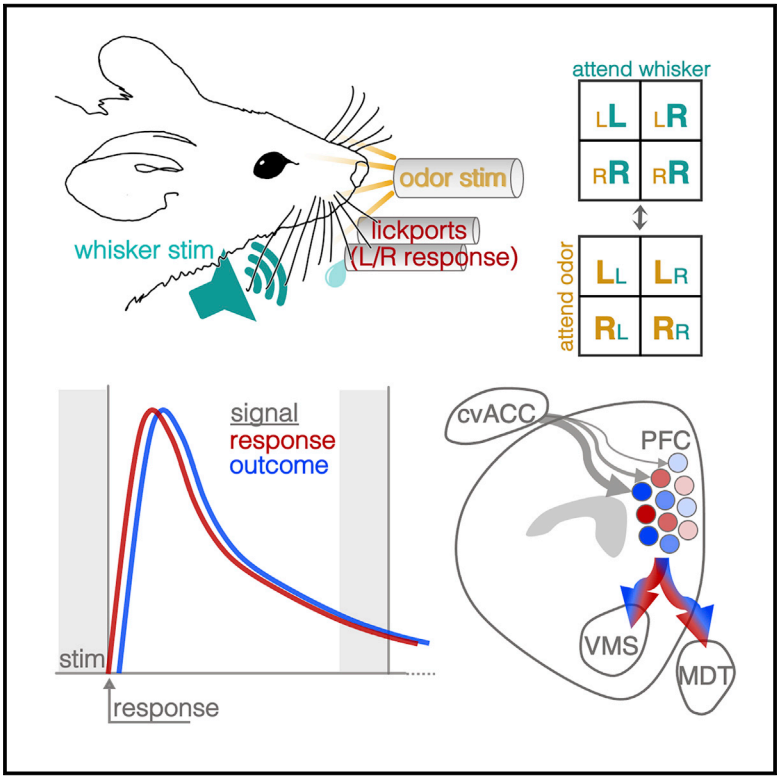

Authors

Timothy Spellman, Malka Svei, Jesse Kaminsky, Gabriela Manzano-Nieves, Conor Liston

Correspondence

tis2013@med.cornell.edu (T.S.), col2004@med.cornell.edu (C.L.)

In brief

The prefrontal cortex of mice supports cognitive flexibility necessary for updating learned behavior by encoding feedback representation of recent trial outcomes in a laminar gradient with deep projection neurons more selective for feedback information, enabling attentional set-shifting by relaying feedback information to downstream targets.

Highlights

- Prefrontal cortical neurons enable attentional set-shifting
- This activity critically encodes feedback from recent trial outcomes
- Two outputs pathways encode parallel feedback information to downstream targets
- Feedback representation in both cell types follows a laminar gradient

Spellman et al., 2021, Cell *184*, 1–17
May 13, 2021
https://doi.org/10.1016/j.cell.2021.03.047

Cell

CellPress

Article

Prefrontal deep projection neurons enable cognitive flexibility via persistent feedback monitoring

Timothy Spellman,[1,2,*] Malka Svei,[1,2] Jesse Kaminsky,[1,2] Gabriela Manzano-Nieves,[1,2] and Conor Liston[1,2,3,*]
[1]Feil Family Brain and Mind Research Institute, Weill Cornell Medicine, New York, NY 10021, USA
[2]Department of Psychiatry, Weill Cornell Medicine, New York, NY 10021, USA
[3]Lead contact
*Correspondence: tis2013@med.cornell.edu (T.S.), col2004@med.cornell.edu (C.L.)
https://doi.org/10.1016/j.cell.2021.03.047

SUMMARY

Cognitive flexibility, the ability to alter strategy according to changing stimulus-response-reward relationships, is critical for updating learned behavior. Attentional set-shifting, a test of cognitive flexibility, depends on the activity of prefrontal cortex (PFC). It remains unclear, however, what role PFC neurons play to support set-shifting. Using optogenetics and two-photon calcium imaging, we demonstrate that medial PFC activity does not bias sensorimotor responses during set-shifting, but rather enables set-shifting by encoding trial feedback information, a role it has been known to play in other contexts. Unexpectedly, the functional properties of PFC cells did not vary with their efferent projection targets. Instead, representations of trial feedback formed a topological gradient, with cells more strongly selective for feedback information located further from the pial surface, where afferent input from the anterior cingulate cortex was denser. These findings identify a critical role for deep PFC projection neurons in enabling set-shifting through behavioral feedback monitoring.

INTRODUCTION

Cognitive flexibility, the ability to respond to changing environmental contingencies, is helpful for navigating through dynamic environments. A form of cognitive flexibility frequently used in clinical assessments is attentional set-shifting, a kind of task-switching behavior that requires a subject to ignore a previously relevant stimulus feature and instead attend to a previously irrelevant feature (Heisler et al., 2015; Tait et al., 2014).

Set-shifting impairments are common in a range of psychiatric disorders (Ceaser et al., 2008; Disner et al., 2011; Halleland et al., 2012; Jazbec et al., 2007; Murphy et al., 2012) and often persist after treatment in both depression and schizophrenia, despite remission of other symptoms (Bortolato et al., 2016; Gonda et al., 2015; Harvey et al., 2004). A long-standing body of evidence indicates that the prefrontal cortex (PFC) plays a critical role in supporting set-shifting behavior in human (Kim et al., 2012; Milner, 1963) and rodent (Birrell and Brown, 2000; Bissonette et al., 2013; Brigman et al., 2005) models, but the physiological mechanisms that enable set-shifting remain poorly resolved.

The dominant model for the role of PFC in set-shifting, which has drawn on support from numerous high-impact publications over the past three decades (Miller and Cohen, 2001; MacDonald et al., 2000; Corbetta and Shulman, 2002; Desimone and Duncan, 1995; Birrell and Brown, 2000; Schmitt et al., 2017), holds that the PFC supports set-shifting by encoding abstract task rules and attentional sets that mediate top-down control of sensorimotor processing and decision-making. Neural activity in primate PFC encodes abstract contextual or rule-related information (Hyman et al., 2012; Mante et al., 2013; Rigotti et al., 2013), and in rodents performing set-shifting tasks, such rule-related representations can shift flexibly with repeatedly changing stimulus-reward contingencies (Durstewitz et al., 2010; Mante et al., 2013; Rich and Shapiro, 2009; Rodgers and DeWeese, 2014; Siniscalchi et al., 2016). Together, these studies suggest that PFC activity might provide an attentional filter that biases sensorimotor responses during set-shifting (Wimmer et al., 2015)—a well-predicated but unproven hypothesis.

Importantly, set-shifting tasks are typically uncued, mirroring the need for uncued adaptations to changing environmental contingencies in the real world; so, set-shifting performance requires continuous trial-and-error learning. Thus, an alternative and not mutually exclusive hypothesis is that PFC supports set-shifting by monitoring feedback in response to recent decisions. In addition to encoding context, prefrontal activity has been shown to represent feedback signals associated with trial outcomes (Bissonette and Roesch, 2015; Starkweather et al., 2018), and recent evidence suggests that such feedback-related activity is important for task-switching behavior (Biró et al., 2019; Ellwood et al., 2017). Whether PFC activity supports set-shifting through

Please cite this article in press as: Spellman et al., Prefrontal deep projection neurons enable cognitive flexibility via persistent feedback monitoring, Cell (2021), https://doi.org/10.1016/j.cell.2021.03.047

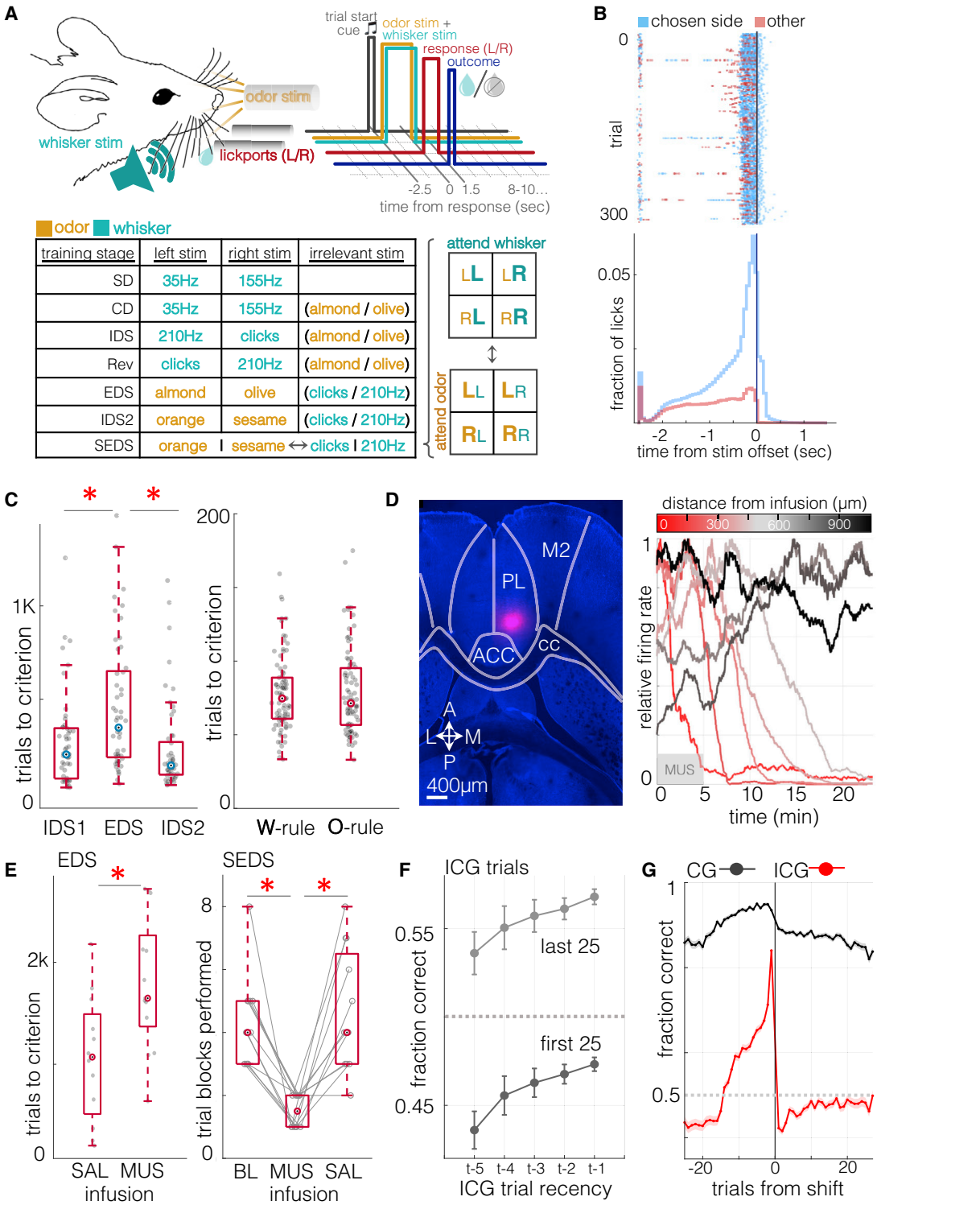

Figure 1. A prefrontal-dependent serial set-shifting task for head-fixed mice

(A) Task schematic. Top left: diagram of stimulus delivery and lick response configuration. Top right: trial sequence (see Results and Star Methods). Bottom: a table of the discrete training stages culminating in the serial extra-dimensional set-shifting task. SD, simple discrimination; CD, compound discrimination; IDS, intradimensional shift; Rev, reversal; EDS, extradimensional shift; IDS2, second intradimensional shift; SEDS, serial extradimensional shift.

(legend continued on next page)

Please cite this article in press as: Spellman et al., Prefrontal deep projection neurons enable cognitive flexibility via persistent feedback monitoring, Cell (2021), https://doi.org/10.1016/j.cell.2021.03.047

feedback monitoring or through attentional modulation of sensorimotor responses is unclear.

It is also unclear how distinct circuit elements interact within PFC to support set-shifting. A major set of questions in behavioral neuroscience in recent years has centered on how best to define anatomical markers of cell types within cortex. Are the functional/coding properties of a given pyramidal neuron determined by its *efferent connectivity* or by its laminar location, a correlate of its *afferent connectivity* (Adesnik and Naka, 2018; Harris and Shepherd, 2015). These two possibilities are not mutually exclusive, and the fact that neuronal subpopulations with distinct efferent connectivity profiles are often found in distinct cortical layers makes it hard to disambiguate the relative contributions of these two factors. While findings from numerous recent studies implicate both laminar location and efferent connectivity in determining the functional properties of pyramidal neurons (Lui et al., 2021; Marshel et al., 2019; Otis et al., 2017; Senzai et al., 2019; Sharif et al., 2021), to disambiguate these two factors requires an experimental preparation that controls for both.

The critical contribution of PFC activity to set-shifting may be mediated by a number of output pathways, but two PFC projection targets of particular interest are the projection to ventromedial striatum (PFC-VMS) and to the mediodorsal thalamus (PFC-MDT). In rodents, both target structures have established roles in set-shifting behavior (Aoki et al., 2015; Block et al., 2007; Floresco et al., 2006; Kato et al., 2018), and PFC projections to both structures underlie behavior that relies on cognitive flexibility (Marton et al., 2018; Nakayama et al., 2018). However, it is unknown whether PFC projections to these downstream targets convey similar or distinct task-critical information during set-shifting.

To address these questions, we developed and validated a novel set-shifting task for head-fixed mice to enable two-photon imaging during serial attentional set-shifts spanning hundreds of trials. While PFC neural activity encoded all essential task features, neural signals encoding the animal's response were detected only *after* trial completion, supporting a role for PFC cells in feedback monitoring rather than attentional biasing of sensorimotor responses. This feedback signal persisted through four subsequent trials, spanning up to 55 s. Separate analysis of PFC-VMS and PFC-MDT neurons revealed strikingly similar representations of all task-related features in both cell types. Unexpectedly, whereas optogenetic inhibition of either cell type had no effect on performance when delivered *during trials*, inhibition during the *post-trial epoch* did impair performance, confirming that the role of these neurons in set-shifting was feedback monitoring and not attentional modulation of sensorimotor responses. Furthermore, while the functional properties of PFC cells did not vary with their efferent projection targets in this context, we found that representations of trial feedback formed a topological gradient, with cells more strongly selective for feedback information located further from the pial surface and receiving denser afferent inputs from the caudo-ventral anterior cingulate cortex (ACC). Together, these findings reveal a critical role for deep PFC projection neurons in supporting set-shifting by relaying feedback information to downstream targets.

RESULTS

A cross-modal set-shifting task for head-fixed mice

Water-restricted mice were presented on each trial with one of two possible whisker vibration stimuli (e.g., 35 versus 155 Hz vibration presented bilaterally) and one of two possible odor stimuli (e.g., almond oil versus olive oil), in randomized combinations, cueing them to respond by licking a left or right lick port to retrieve a water reward upon termination of the 2.5 s compound stimulus (Figures 1A and 1B). In alternating trial blocks, either whisker or odor stimuli signaled the location of the reward. As in most set-shifting tasks (Bissonette et al., 2008; Tait et al., 2014), animals underwent a standardized series of task transitions to expose them to multiple exemplars from each stimulus modality and build an attentional set: simple discrimination (SD), in which animals were trained to discriminate between two stimuli within a single sensory modality; compound discrimination (CD), in which a distractor stimulus from the untrained sensory modality was added; intradimensional shift (IDS), in which the stimuli from the relevant sensory modality were replaced with a new pair of exemplars; reversal (Rev), in which the left/right mapping was switched; extradimensional shift (EDS), in which the rule changed for the first time so that the pair of stimuli from the previously *irrelevant* sensory modality became the *relevant* stimuli; a second IDS (IDS2), in which the pair of stimuli from the *newly relevant* sensory modality was replaced with a new pair of exemplars; and finally, serial

(B) Summary of licking behavior. Top: rasterized and trial-aligned lick times for an example session. Bottom: summary lick time histogram (655,236 licks; 150 sessions; 32 animals). In 95% of trials, the choice lick (first lick made after stimulus termination) came in the first 0.346 ms of the response window, a latency equal to a single frame of imaging.

(C) Left: number of trials to criterion, IDS versus EDS, N = 53 animals. Signed rank $z = -2.9$, $p = 0.0034$ for IDS/EDS; $z = -4.0$, $p = 6 \times 10^{-5}$ for IDS2/EDS; $z = 1.4$, $p = 0.15$ for IDS/IDS2. Right: mean trials to criterion during SEDS sessions, whisker rule versus odor rule. N = 115 animals, signed rank $z = 0.14$, $p = 0.9$.

(D) Muscimol infusion in PFC. Left: horizontal section (−1.95 mm ventral from brain surface at anterior-posterior, medial-lateral [AP/ML] bregma, fluorescent muscimol). Right: relative multiunit firing rate (proportion of channel maximum, 0.5 Hz bins, 100 s moving average).

(E) Left: trials to criterion in EDS sessions during transcranial infusion (saline [SAL], muscimol [MUS]). N = 12, 13 mice (SAL, MUS). Rank sum $z = 2.4$, $p = 0.02$. Right: number of trial blocks reaching criterion performance in SEDS sessions following 10 rule shifts. N = 12; median blocks (BL, baseline; MUS, muscimol; SAL, saline): 4, 1.5, 4. Signed rank $p = 0.0005$ (BL/MUS), 0.001 (SAL/MUS), 0.68 (BL/SAL). Median total trials completed: SAL = 644; MUS = 651; signed rank $p = 0.52$.

(F) Incongruent trial performance by recency of previous incongruent trial during SEDS sessions (mean ± SEM). Top: performance during the last 25 trials of trial blocks, prior to reaching criterion. Bottom: performance during the first 25 trials of trial blocks, after undergoing rule shifts. N = 693 sessions in 131 animals. ANOVA for ICG trial recency versus ICG trial performance: $t = -4.68$, $p = 3 \times 10^{-6}$.

(G) SEDS trial performance relative to rule shift, mean ± SEM. Same sessions as in (F). Note that because trial shifts were triggered by criterion performance, correct response rates immediately following the rule shift are a better estimate of true performance than trials immediately preceding the shift.

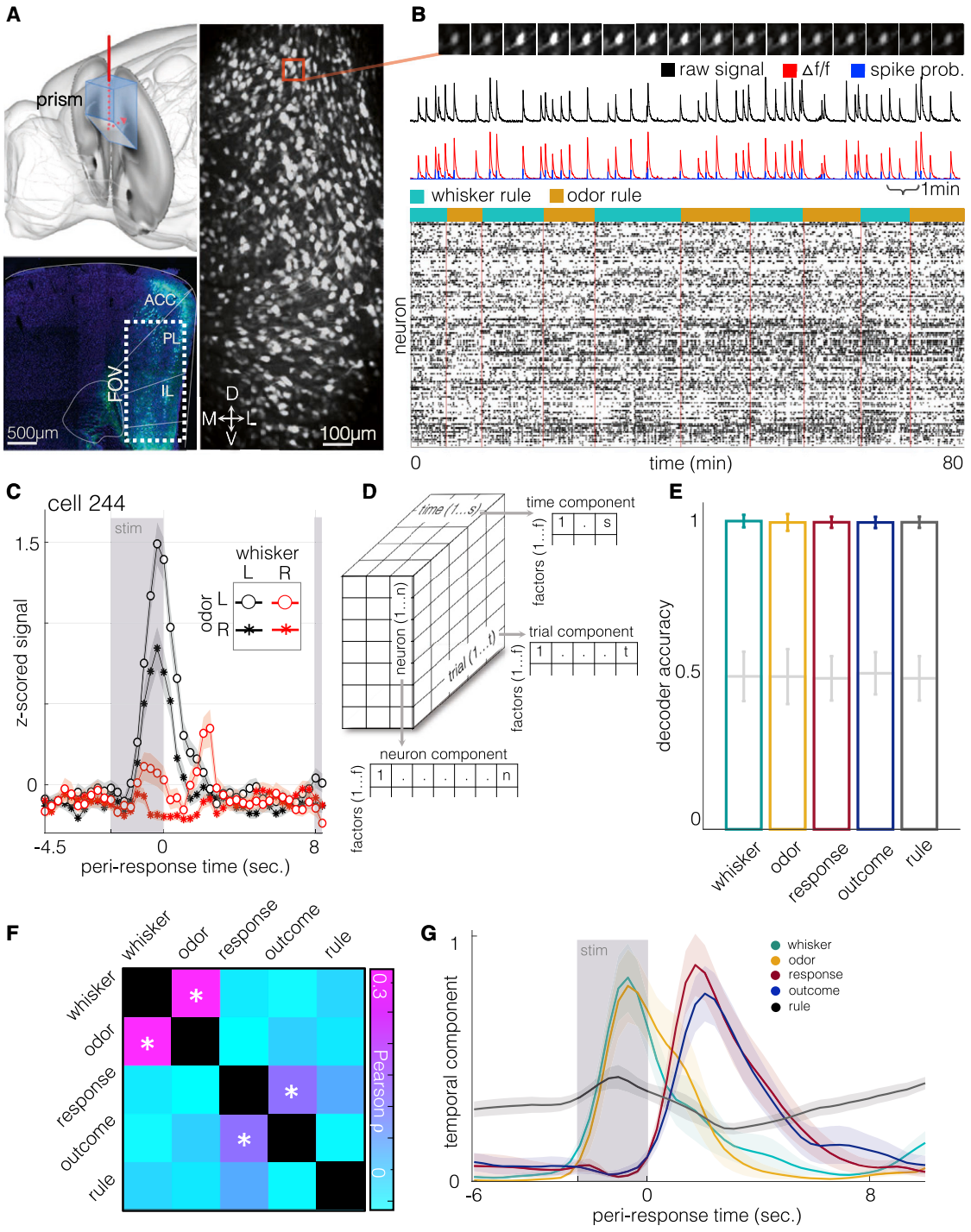

Figure 2. Prefrontal representation of task variables in population activity

(A) Top left: schematic of coronal prism implantation field. Field-of-view (FOV) bregma coordinates: AP +1.85 mm, ML 0–0.75 mm left, dorsal-ventral (DV) 1.0–2.5 mm from brain surface. Bottom left: hSyn-GCaMP6f fluorescence in fixed tissue (DAPI in blue). Right: standard deviation image from 115 min hSyn-GCaMP6f recording (2.89 Hz, N = 953 units).

(B) Example frames, traces, and putative spike times from calcium imaging sessions. Top: 16 frames of a calcium transient from an example neuron in (A). Frames downsampled by a factor of 2. N = 100 units recorded over the course of 10 trial blocks.

(C) Mean ± SEM of Z scored activity for all trials from an example neuron during trials with four stimulus combinations (*whisker stimulus* 35 Hz/155 Hz, *odor stimulus* olive/sesame). Stimulus is presented from −2.5 to 0 s. Earliest subsequent trial onset at 8 s.

(D) Schematic of TCA rank decomposition.

(legend continued on next page)

Please cite this article in press as: Spellman et al., Prefrontal deep projection neurons enable cognitive flexibility via persistent feedback monitoring, Cell (2021), https://doi.org/10.1016/j.cell.2021.03.047

extradimensional shift (SEDS), in which the rule switched automatically whenever the animal reached criterion performance, which was 80% correct within a 30-trial moving window and >50% on both left and right trials (Figure 1A; see STAR Methods for details). Infusion of muscimol within PFC (Figure 1D) impaired set-shifting performance, increasing trials to criterion in the initial EDS shift as well as after completing 10 shifts of SEDS (Figure 1E).

Trials belonged to two classes, which were randomized from trial to trial: those in which the whisker and odor rules cued the same response direction (congruent [CG] trials) and those in which the whisker and odor rules cued opposing response directions (incongruent [ICG] trials). Therefore, ICG trials, but not CG trials, required application of the modality rule, and feedback from ICG trials alone carried information about modality rule. Animals used prior ICG trial information to guide behavior, so that ICG trial performance was enhanced following feedback from a recent ICG trial, and this held true in trials occurring both early and late within trial blocks (Figure 1F).

Set-shifting task variables represented in prefrontal population activity

To measure task-related activity in PFC neurons, GCaMP6f-mediated two-photon calcium imaging was performed through a coronally implanted microprism (Andermann et al., 2013; Low et al., 2014), producing a field of view that preserved cortical laminar structure and comprised prelimbic and infralimbic areas (Figures 2A, 2B, and S7A). GCaMP was expressed pan-neuronally (hSyn-GCaMP6f) or in specific projection neuron subtypes (hSyn-DIO-GCaMP6f and rAAV2-Cre in PFC-VMS and PFC-MDT). Although these cell types were subsequently analyzed separately, we began by characterizing the task responsiveness of all labeled neurons.

We used tensor component analysis (TCA; Figure 2D) to decompose the neural data into low-rank factors defined as related sets of weights in the neuron, trial, and time point (within-trial) dimensions (Williams et al., 2018). Because this dimensionality reduction technique separates trial and time point components, it allowed for variables to be directly compared with each other, regardless of when their peak representation occurred within the trial. Using the trial components as inputs to a support vector machine (SVM)-based maximum-margin linear decoder (Christianini and Shawe-Taylor, 2000; Meyers et al., 2008), trials were classified according to *whisker stimulus* (e.g., clicks versus 210 Hz), *odor stimulus* (e.g., almond versus olive), *response* (left/right), *outcome* (correct/incorrect), and *rule* (attend whisker or odor) with near perfect accuracy in held-out test data (Figure 2E; see also Figure S7 and STAR Methods for model parameterization).

General linear model (GLM) coefficients for *whisker* and *odor stimuli* were significantly correlated with each other across factors, as were *response* and *outcome*, indicating these pairs of variables were encoded by similar activity patterns (Figure 2F). One way this could manifest is if activity patterns encoding *whisker* and *odor* follow overlapping temporal trajectories within the trial, and likewise for *response* and *outcome*. To determine the trial-aligned time courses of the factors associated with the task variables, we plotted the TCA-derived temporal components of the factors most strongly associated with each variable (Figure 2G). Temporal components associated with *whisker* and *odor stimulus* peaked during stimulus presentation, while components associated with *outcome* peaked during the subsequent inter-trial interval (ITI). Notably, components associated with *response* followed a temporal trajectory that was similar to *outcome*, peaking after the end of the trial. These results demonstrate that all task elements necessary for successfully executing the task are represented in PFC neuronal population activity; that activity patterns associated with *response* are more correlated with those associated with *outcome* than with those associated with the decision-related stimuli; and that the *response*-associated patterns lag, rather than lead, the animal's behavioral choice.

Response and outcome representations in post-trial activity

Because the TCA-based population analysis revealed signals encoding *response* and *outcome* in the post-trial ITI, we wondered whether these variables might continue to be represented in the neural signal beyond the start of the subsequent trial. To answer this question, we used GLM regression to model activity rates in individual neurons as a function of *whisker stimulus*, *odor stimulus*, *response, outcome*, and *rule*, with the addition of the variables *previous trial response* and *previous trial outcome*. Analysis of the mean GLM coefficients at each time point (Figure 3C) revealed that coefficient values for *response* and *outcome* peaked at a mean of 1.73 and 2.42 s after stimulus offset, respectively, and remained elevated above chance through the following trial.

Given that animals required 15–20 incongruent trials to abandon a rule after an uncued rule change (Figure 1E), we looked for signs of outcome-related evidence accumulation that spanned multiple trials, as has been reported in reinforcement learning tasks (Bari et al., 2019; Bernacchia et al., 2011; Siniscalchi et al., 2019). We ran linear decoders on *whisker* and *odor stimuli*, *response*, and *outcome* for past trials and found that, while *whisker* and *odor* representations were no longer detectable after one trial, *response* and *outcome* representations persisted for up to four trials, or up to 55 s (Figure 3D).

Do these *response* and *outcome* signals reflect the demands of the uncued set-shifting task, or are they natively expressed during decision-making more generally? To answer this question, we

(E) Support vector machine (SVM) decoder accuracy for five task-related features. Trial factors obtained from TCA decomposition (35 factors) were used as inputs to a SVM-based decoder. N = 4,740 neurons from 21 animals. Error bars represent standard deviations. Gray plots, shuffled labels.
(F) Cross-correlation of task feature representation in TCA trial space. GLM regression was performed on the five task variables, using TCA factors as predictors. Pearson correlation was then performed on the resulting coefficients (same data as in E). Asterisks indicate $p < 0.01$.
(G) Time components from significantly modulated factors. For each of the five task variables, factors most strongly modulated by each task variable are shown in the temporal domain (mean ± SEM for each variable, N = 16 factors for *whisker stimulus*, N = 12 factors for *odor stimulus*, N = 26 factors for *response*, N = 21 factors for trial *outcome*, N = 59 factors for *rule*).

Please cite this article in press as: Spellman et al., Prefrontal deep projection neurons enable cognitive flexibility via persistent feedback monitoring, Cell (2021), https://doi.org/10.1016/j.cell.2021.03.047

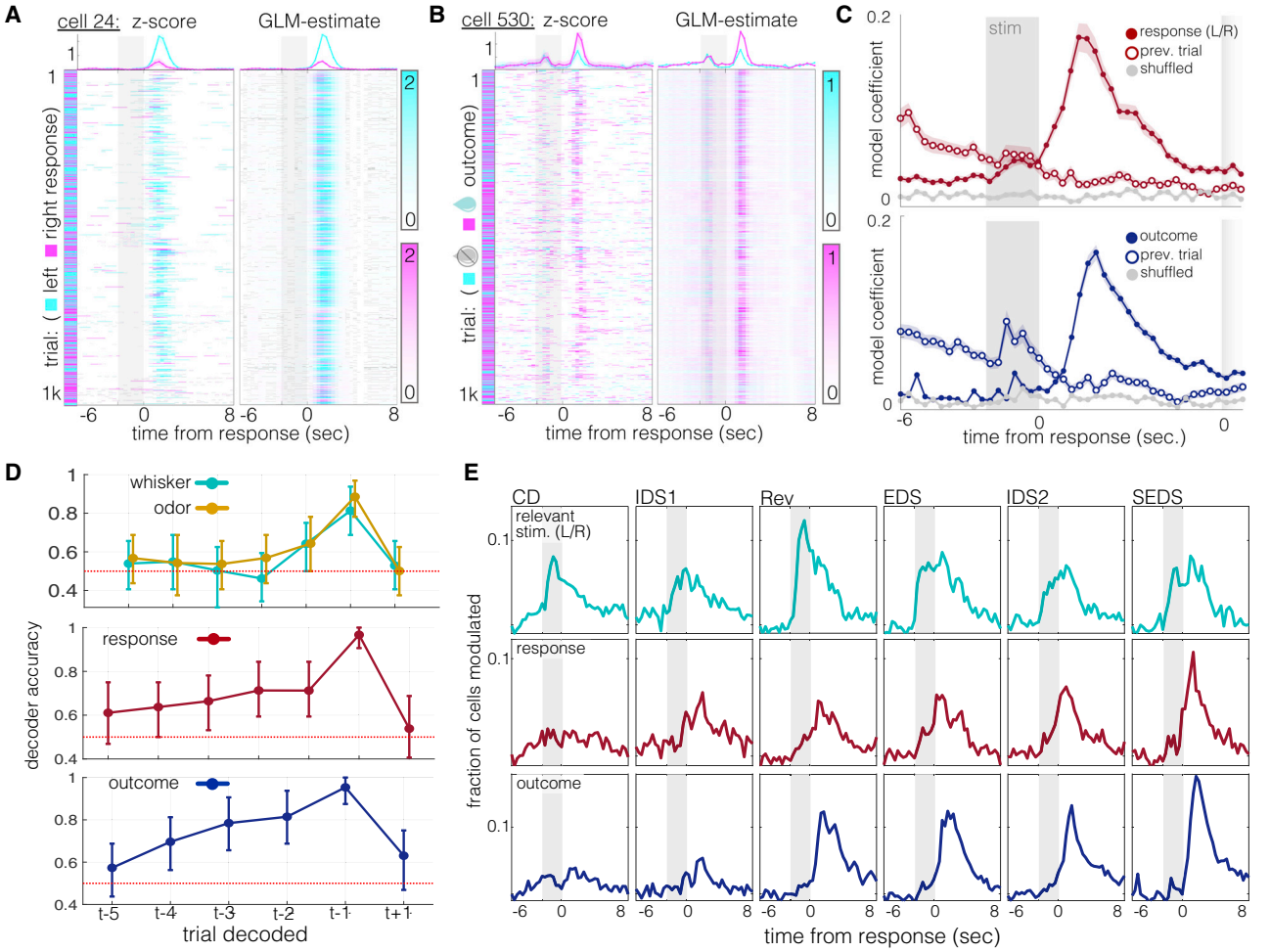

Figure 3. Task-related *response* and *outcome* representations in post-trial activity

(A) Example neuron with selectivity for *response* in its post-trial activity. Left: Z scored activity. x axis, time within trial (gray box: stimulus presentation window, −2.5 to 0 s). y axis: trial number (1,071 trials total). Right: GLM estimate for time-aligned activity. Cyan: trials in which the animal chose left; magenta: trials in which the animal chose right. Top: mean ± SEM traces from each trial condition. Top y axis units are Z scored activity.

(B) Same format as in (A) for an example neuron selective for trial *outcome*. Cyan: incorrect trials; magenta: correct trials.

(C) Trial-aligned GLM coefficients for neurons significantly modulated by *response* (top) and trial *outcome* (bottom). Modulated neurons include those with significant modulation at any time point (Bonferroni corrected for the 43 trial time points). Closed circles: mean ± SEM of coefficients for currently trial; open circles: mean ± SEM of coefficients for previous trial. Gray traces: coefficients from GLMs on shuffled data. N = 285 neurons for *response* and 756 for trial *outcome* of 4,730 total neurons from 21 animals.

(D) Means ± 95% confidence intervals (CIs) for SVM decoders tested on past (t-...) and future (t+...) trial features. Top: decoders for *whisker* and *odor stimulus*. Middle: decoders for *response*. Bottom: decoders for trial *outcome*. Red dashes: chance performance.

(E) Histograms: fraction of neurons significantly modulated (same GLM as in A–C) by task features over trial-aligned time points and through learning stages. Top row: fraction of neurons modulated by the relevant stimulus. Middle row: *response*. Bottom row: trial *outcome*.

tracked these signals across learning stages. Signals corresponding with the relevant stimulus were present from the earliest recorded session (CD) and remained strong throughout all subsequent task stages (Figure 3E, top row). Conversely, *response*- and *outcome*-related activity emerged only over the course of multiple task transitions (Figure 3E, rows 2 and 3).

A circuit-level mechanism representing outcomes across multiple trials in a stable, colinear activity space

That trial feedback information could be decoded for up to four trials in the past led us to question how these past trials were encoded: were these representations stable, maintained by consistent groups of neurons, or maintained by groups whose membership shifted over time? We first examined the stability of *outcome* selectivity across sessions and found that *outcome* is represented by relatively stable groups of neurons over days (Figures 4A–4C).

We then examined the temporal stability of *outcome* signals over trials. The neurons responsible for coding a given trial *outcome* might shift between trials, with different groups of neurons inheriting representations of different past trials. Alternatively, these trial histories might be multiplexed by the same

Please cite this article in press as: Spellman et al., Prefrontal deep projection neurons enable cognitive flexibility via persistent feedback monitoring, Cell (2021), https://doi.org/10.1016/j.cell.2021.03.047

CellPress

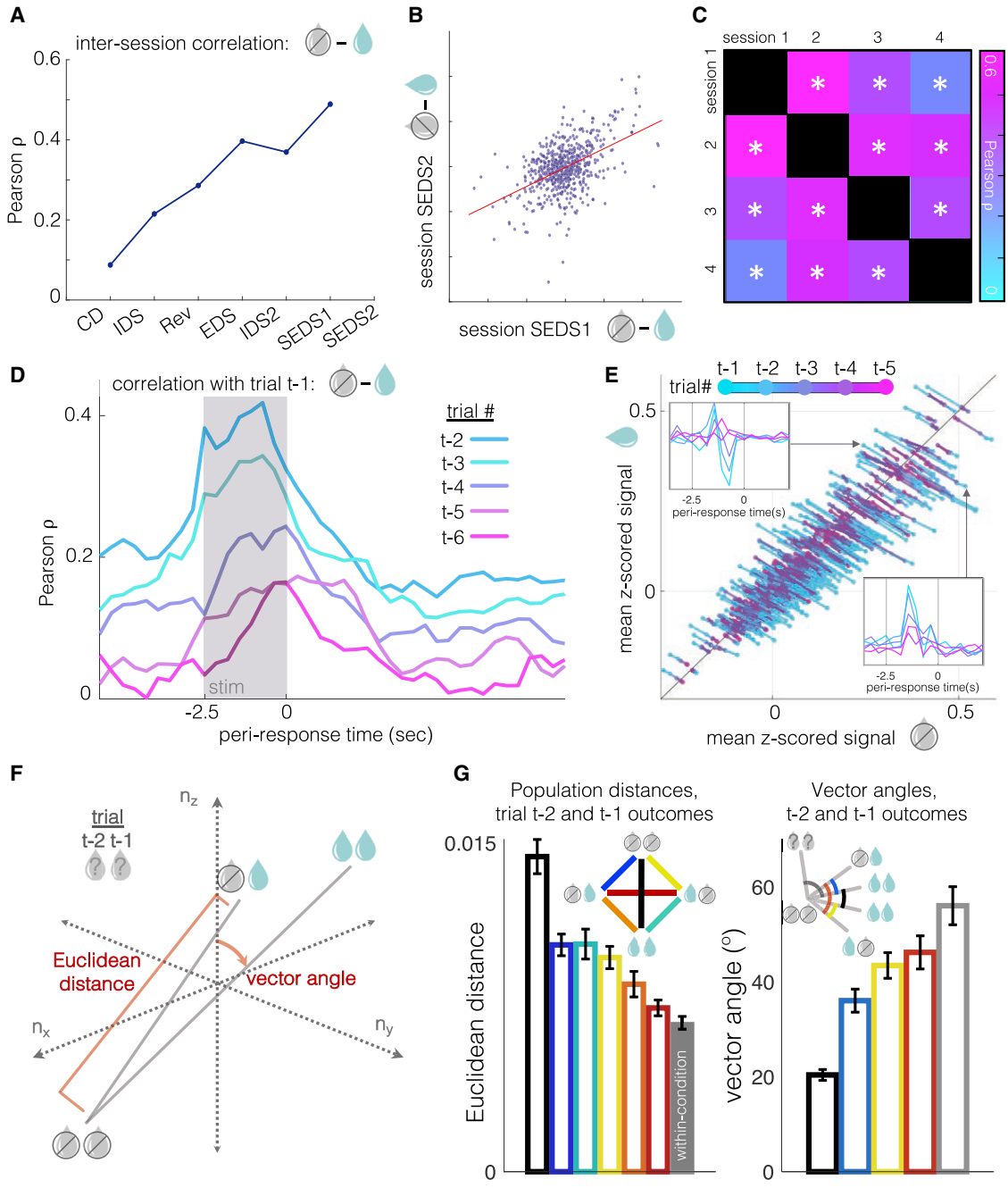

Figure 4. Outcomes are represented across multiple trials in a stable, colinear activity space

(A) Inter-session correlation of trial *outcome* representation (neurons significantly modulated in at least one session, rank sum, $p < 0.05$). From CD to IDS, N = 1,083 neurons in 17 animals; from IDS to Rev, 1,543 neurons in 16 animals; from Rev to EDS, 1,382 neurons in 15 animals; from EDS to IDS2, 1,443 neurons in 15 animals; from IDS to the first SEDS session, 1,519 neurons in 21 animals; from the first to second SEDS sessions, 635 neurons in 21 animals.

(B) Scatterplot of *outcome* selectivities for individual, significantly modulated neurons in the first and second SEDS sessions (same neurons as in A). Pearson R = 0.49, $p = 1.6 \times 10^{-39}$. Correlation for all neurons (unmodulated as well as modulated) was 0.36, $p = 7.5 \times 10^{-60}$, N = 1,959 neurons.

(C) Similarity of *outcome* selectivity over multiple SEDS sessions (173 neurons, from 8 animals, recorded in at least four consecutive behavioral sessions). Neurons significantly modulated by trial *outcome* in at least one session (rank sum $p < 0.05$) were included, although analysis of all neurons produced comparable results (1,091 neurons, R = 0.17–0.38, all $p < 1 \times 10^{-7}$).

(D) Trial-aligned correlation coefficients comparing *outcome* selectivity (defined as in A–C) between trial t-1 and trials t-2 through t-6. N = 4,740 cells from 21 animals. Gray box: stimulus presentation.

(E) A time-compressed representation of the results from (D), broken out by individual neurons. x axis: mean activity on incorrect trials; y axis: mean activity on correct trials. Insets: example cells preferring correct (top) and incorrect (bottom) *outcome* in trials t-1 to t-5.

(legend continued on next page)

Please cite this article in press as: Spellman et al., Prefrontal deep projection neurons enable cognitive flexibility via persistent feedback monitoring, Cell (2021), https://doi.org/10.1016/j.cell.2021.03.047

neurons, whose activity could be incrementally modulated with each correct and incorrect trial. To test these possibilities, we compared *outcome* selectivities for successive past trials and found that they were indeed supported by correlated populations, whereby, e.g., neurons excited by reward in trial t-1 were also excited by reward in trial t-2 (Figures 4D–4G). Together, these results define a coding scheme in which a subset of PFC neurons represent the *outcome* of each trial, with their activity state modulated in an incremental, relatively colinear way, with decreasing amplitude as trials recede into the past, rather than different groups of neurons representing *outcomes* at different latencies from each trial.

Similar task responsiveness in two major PFC projection neuron populations

Our above-mentioned findings indicate that PFC cells are highly functionally heterogeneous with respect to their contributions to cognitive flexibility in this set-shifting paradigm. To understand the mechanistic basis of this functional heterogeneity, we questioned whether the task-related activity of a PFC neuron might be a function of its long-range efferent connectivity profile or of its laminar location, a correlate of afferent connectivity. While not mutually exclusive, these two proposed correlates of functional specialization within cortex have motivated numerous studies in recent years, and noteworthy findings have lent support to both hypotheses.

To examine the degree to which projection target specificity contributed to the functional heterogeneity of in PFC neurons during set-shifting, we examined the functional properties PFC-VMS and PFC-MDT neurons, two projection-defined PFC output populations whose target structures have both been implicated in supporting cognitive flexibility in prior work (Block et al., 2007; Floresco et al., 2006; Marton et al., 2018). Labeling of both populations within the same animals (Soudais et al., 2001; Tervo et al., 2016), using rAAV-Cre labeling, revealed two largely non-overlapping cell types that were also spatially intermingled (Figures 5A and 5B). Despite this sparse cross-labeling, examination of fluorescent axons in labeled neurons from the two groups (Figures 5C and 5D) revealed two distinct populations (Figures 5E and S5), and SVM linear decoders trained to classify injection type, based on the labeling densities in the target regions presented in Figure 5E, performed with 100% accuracy on held-out test data from each animal.

Contrary to our expectations, the two populations showed a striking degree of overall similarity in their task responsiveness (Figure 5F). Both populations showed modulation by trial *outcome* that emerged through successive learning stages (Figure 5G). Similar distributions of neurons in each population were excited versus inhibited by trial onset (Figure 5H), and the two cell types each showed comparable distributions of correct-preferring and incorrect-preferring neurons (Figure 5I). Principal component analysis showed similar trial-aligned temporal profiles for the main components (Figure 5J). Together, these results show that while individual PFC neurons are highly heterogeneous in their functional properties, efferent projection targets do not account for this functional heterogeneity in these two major projection subtypes.

Interference with feedback monitoring in PFC projection populations impairs set-shifting

The finding of durable representations of trial feedback signals over successive trials raised the possibility that the task-critical role of the PFC might be feedback monitoring. However, the robust representation of *whisker/odor stimuli* and *rule*, particularly during stimulus presentation, tended to support the prevailing model of PFC involvement in set-shifting, namely that PFC activity controls top-down, attention-mediated biasing of rule-dependent action selection in the task. We next tested these possibilities using projection-targeted optogenetics.

We used the soma-targeted, anion-conducting channelrhodopsin stGtACR2 (Mahn et al., 2018) to inhibit PFC activity (Figure 6A). Photoactivation of the channel across a 10-fold range of light intensities produced strong silencing of spiking activity in extracellular recordings (Figure 6B). Next, we tested the requirement of PFC activity for successful set-shifting performance in three temporally controlled stimulation regimes: during trials (0.5 s trial-ready cue period, 2.5 s stimulus presentation, and $\leq$1.5 s response window), during the ITI (8–10 s epoch triggered on response lick) following CG trials, or during the ITI following ICG trials (Figure 6C). Trial blocks (beginning with rule switch and ending with the animal reaching criterion for the new rule) alternated light off/on.

Photoactivation of pan-neuronally expressed stGtACR2 during the ITI following incongruent trials impaired performance on ICG trials (Figure 6D), but not on CG trials (Figure 6E). No effect of light was seen for control tdTomato-expressing animals (Figures 6D and 6E). This effect was also seen in animals expressing stGtACR2 in PFC-VMS or PFC-MDT projection neurons (Figures 6D and 6E). When light was delivered following CG trials, no impairment was seen on ICG trial performance for either projection population (Figure 6F), indicating that the impairment seen with post-ICG inhibition reflected an interference with prior trial feedback, rather than preparation for the subsequent trial (see also Table S1). Together, these results confirm a critical role for post-trial activity in both PFC-VMS and PFC-MDT neurons in enabling set-shifting.

Strikingly, neither PFC-VMS nor PFC-MDT activity was necessary for execution of the rule-guided response, as no impairment was seen with photoactivation during ICG trials (Figure 6G). In light of this unexpected result, we sought another association

(F) Schematic diagram of Euclidean distance and vector angle computed from trial-averaged *outcome* (correct versus incorrect) conditions in neural activity space.

(G) Left: Euclidean distances for all combinations of trial t-1 and t-2 *outcomes* in N-dimensional activity space (same data as in A–E). Bar heights and error bars are means ± 95% CIs over 500 trial sub-samplings with replacement (50% of trials in one condition, 50% in the other). The rightmost (gray) bar is the mean distance within condition (e.g., [t-1 correct, t-2 correct] versus [t-1 correct, t-2 correct]) across sub-samplings. Right: angles between pairs of trial *outcome* vectors shown at left. All vectors use [t-1 incorrect, t-2 incorrect] as vertex. Bar heights and error bars are mean ± 95% CIs as at left. Leftmost (black) bar is the mean within-condition angle, a proxy for baseline, as more dimensions tend to increase vector angles in noisy data (Brinkman and Charikar, 2005).

Please cite this article in press as: Spellman et al., Prefrontal deep projection neurons enable cognitive flexibility via persistent feedback monitoring, Cell (2021), https://doi.org/10.1016/j.cell.2021.03.047

CellPress

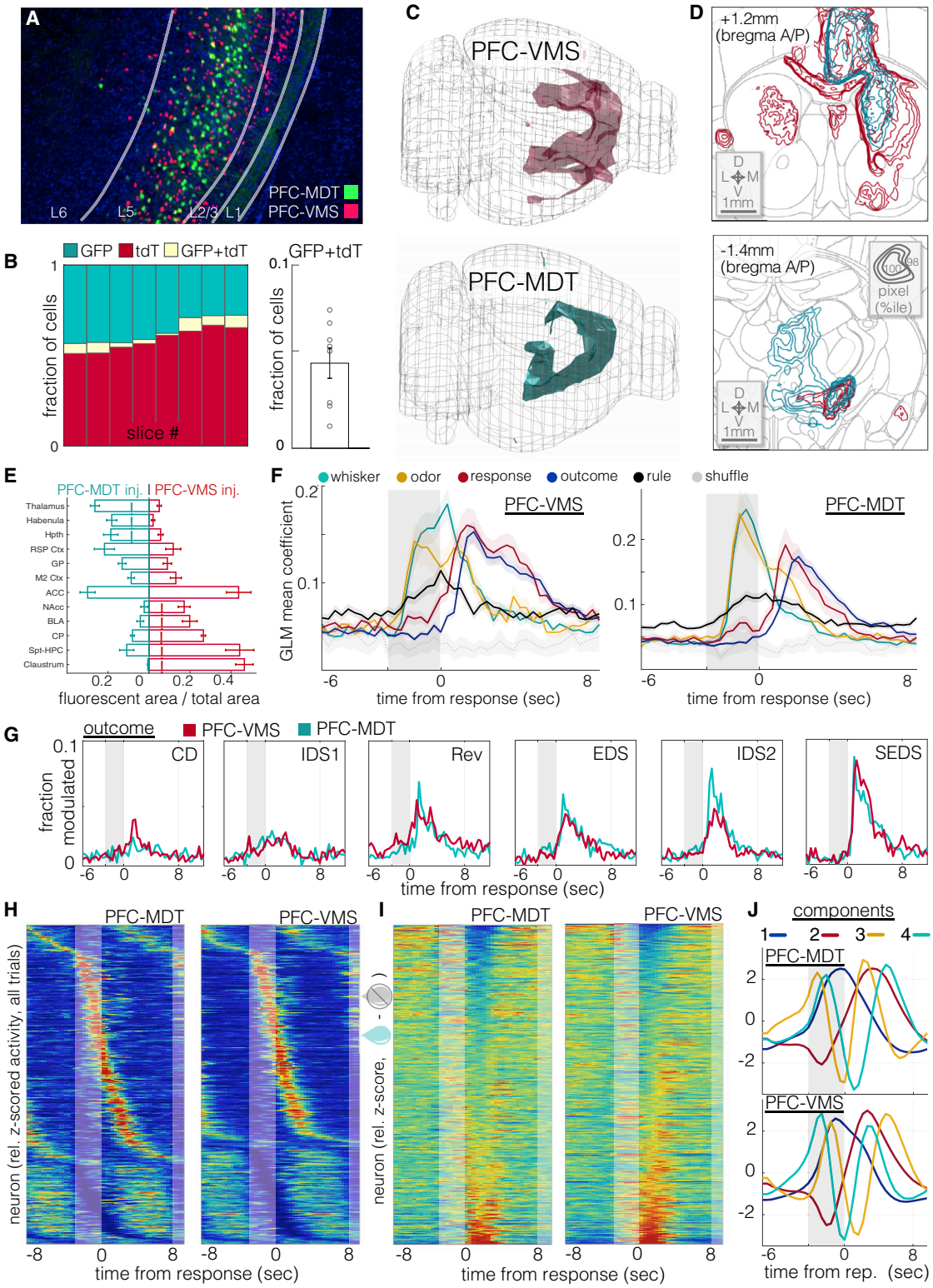

Figure 5. PFC-VMS and PFC-MDT projection populations exhibit similar task response properties

(A) Dual PFC-VMS and PFC-mediodorsal thalamus (MDT) projection labeling in a single preparation. Green: rAAV2-CAG-mGreenLantern in MDT; red: AAV9-CAG-F3/FRT-NLS-tdTomato in PFC and CAV2-FLP in VMS (DAPI in blue).

(B) Cell counts by slice from the experiment in (A). Left: relative green, red, and double-labeled cell counts. Right: median relative overlap (N = 8 sections, 2 animals).

(legend continued on next page)

area that might mediate rule-dependent responding in real-time. We chose the posterior parietal cortex (PPC), which has been previously implicated in cognitive flexibility (Fox et al., 2003; Prado et al., 2017), as well as in monitoring sensory history (Akrami et al., 2018). Silencing of PPC during trials impaired performance on ICG trials, but not on CG trials (Figure 6G), indicating that the PPC mediates responding in the task in a specifically rule-dependent manner, possibly by an attentional mechanism.

Feedback-related activity follows an anatomical gradient, independent of efferent target

The surprising similarity of both task-related activity and the task-critical function of the PFC-VMS and PFC-MDT pathways left open the question of whether the functional heterogeneity of PFC neurons might be explained by their spatial distribution. As has been demonstrated in sensory cortex (Smith and Kohn, 2008), temporal correlations across pairs of simultaneously recorded neurons decayed with distance (Figure 7A), demonstrating an association between spatial proximity and temporal coactivation within the context of the task.

To assess whether neurons' responsiveness to trials varied as a function of their distance from the pial surface, we quantified the population variance of trial-averaged waveforms to capture the magnitudes of neuron responses, including those both excited and inhibited at each time point. More deeply situated neurons (further from pial surface) exhibited greater response magnitude (Figures 7B and 7C).

In addition to trial responsiveness, task-related information was heterogeneously distributed across the cortical laminar axis, with more deeply situated neurons exhibiting greater selectivity for *response* and *outcome* during the ITI (Figures 7D and 7E). We analyzed variance in *response* and *outcome* coding along the dorso-ventral axis, testing for differences between the prelimbic and infralimbic subregions, but we observed no such differences (data not shown).

The findings of greater trial responsiveness and greater selectivity for trial *response* and *outcome* in deeper neurons led us to look for a potential mechanism by which deep neurons might exhibit stronger coding of task-critical variables than superficial neurons. To address whether deep and superficial neurons have differential inputs, we used a rabies tracing approach, targeting EnvA-G-deleted rabies-mCherry to PFC projection neurons in spatially restricted deep or superficial injections (Figure 7F). We began by comparing the distributions of cells labeled by deep versus superficial injections as a function of their distance from the corresponding PFC injection sites. Because this comparison revealed a significant difference that was driven by neurons located between 1 and 2 mm from the PFC injection coordinates (Figure 7G, left), we next identified which regions were occupied by labeled neurons within this range (Figure 7G, inset pie chart). A plurality of labeled neurons in this range were located in the caudo-ventral portion of the ACC, and deep PFC injections labeled more cells in caudo-ventral ACC than superficial PFC injections (Figures 7G, left, and 7H). Although relatively large numbers of labeled cells were seen in secondary motor cortex (M2), caudo-dorsal ACC, and orbitofrontal cortex (OFC, medial + lateral), no significant differences were seen across animals by injection site in these regions. Given that ACC has been identified as an area critical for both set-shifting behavior and reward-related feedback monitoring in previous studies (Bissonette et al., 2013; Hyman et al., 2017), this enriched input from caudo-ventral ACC to deep PFC projection neurons provides a potential source of input driving the stronger representation of trial-feedback-related information seen in the deeper neurons. While other regions showed trends toward differences in the number and spatial distribution of inputs to deep and superficial PFC projection neurons that were evident in data pooled across animals, these differences were not significant across animals (Figure S6).

As a further test of the association between laminar depth and stronger coding of *response* and *outcome* signals, we leveraged the selective viral tropism of two separate PFC-MDT projection populations (Figure 7I): one layer 5 population, for which rAAV2 has strong tropism, heretofore referred to simply as PFC-MDT and hereafter referred to as PFC(L5)-MDT; and one in layer 6, for which canine adenovirus (CAV2) has strong tropism, hereafter referred to as PFC(L6)-MDT (Collins et al., 2018). We used these two viruses as Cre expression vectors to selectively label the two populations with GCaMP6f and compared their selectivity for *response* and *outcome* during

(C) Composite images of long-range axon projections from PFC-VMS (N = 5 animals) and PFC-MDT (N = 5 animals) labeling (see STAR Methods, Videos S3 and S4). Volumes shown are thresholded to $\geq 98^{th}$ percentile for pixel brightness.

(D) Coronal sections and contour plots of fluorescent axon density in PFC-VMS (top) and PFC-MDT (bottom) labeled animals. Top: a composite (N = 5 animals) of pixel brightness in a coronal cross section centered on the nucleus accumbens. Concentric contours correspond with relative pixel brightness. Bottom: composite (N = 5 animals) of pixel brightness in a coronal cross section centered on medial thalamus. Contour brightness scale as in (top).

(E) Mean ± SEM plots showing the fraction of pixels in each region showing fluorescence above the threshold percentile. Two-way ANOVA revealed an interaction effect between injection type and region ($F = 17.96$, $p = 0$). Post hoc t tests revealed significant differences (unpaired t test $p < 0.01$) for thalamus, habenula, caudoputamen, septo-hippocampal complex, and claustrum and $p < 0.02$ for hypothalamus, basolateral amygdala, and nucleus accumbens.

(F) Trial-aligned SVM decoder accuracy for *whisker stimulus, odor stimulus*, *response*, *outcome*, and *rule*. N = 1,770 units from 8 animals (PFC-VMS, left) and N = 1,155 units from 9 animals (PFC-MDT, right).

(G) Histograms traces of the fraction of cells modulated (rank sum $p < 0.01$) by trial *outcome* over trial-aligned time points and through learning stages for PFC-VMS (red) and PFC-MDT (green) neurons.

(H) Trial-averaged activity histograms for PFC-VMS (left) and PFC-MDT (right) cells. Each cell's mean trace is normalized to its peak value, and cells are sorted by time of peak excitation (top) or inhibition (bottom).

(I) Mean *outcome* difference (incorrect − correct) traces for PFC-VMS and PFC-MDT neurons. Each cell's mean difference trace is normalized to its peak value, and cells are sorted from most strongly preferring correct *outcomes* (top) to incorrect *outcomes* (bottom).

(J) First four principal components for trial-averaged activity histograms in PFC-MDT (top) and PFC-MDT (bottom) neurons.

Please cite this article in press as: Spellman et al., Prefrontal deep projection neurons enable cognitive flexibility via persistent feedback monitoring, Cell (2021), https://doi.org/10.1016/j.cell.2021.03.047

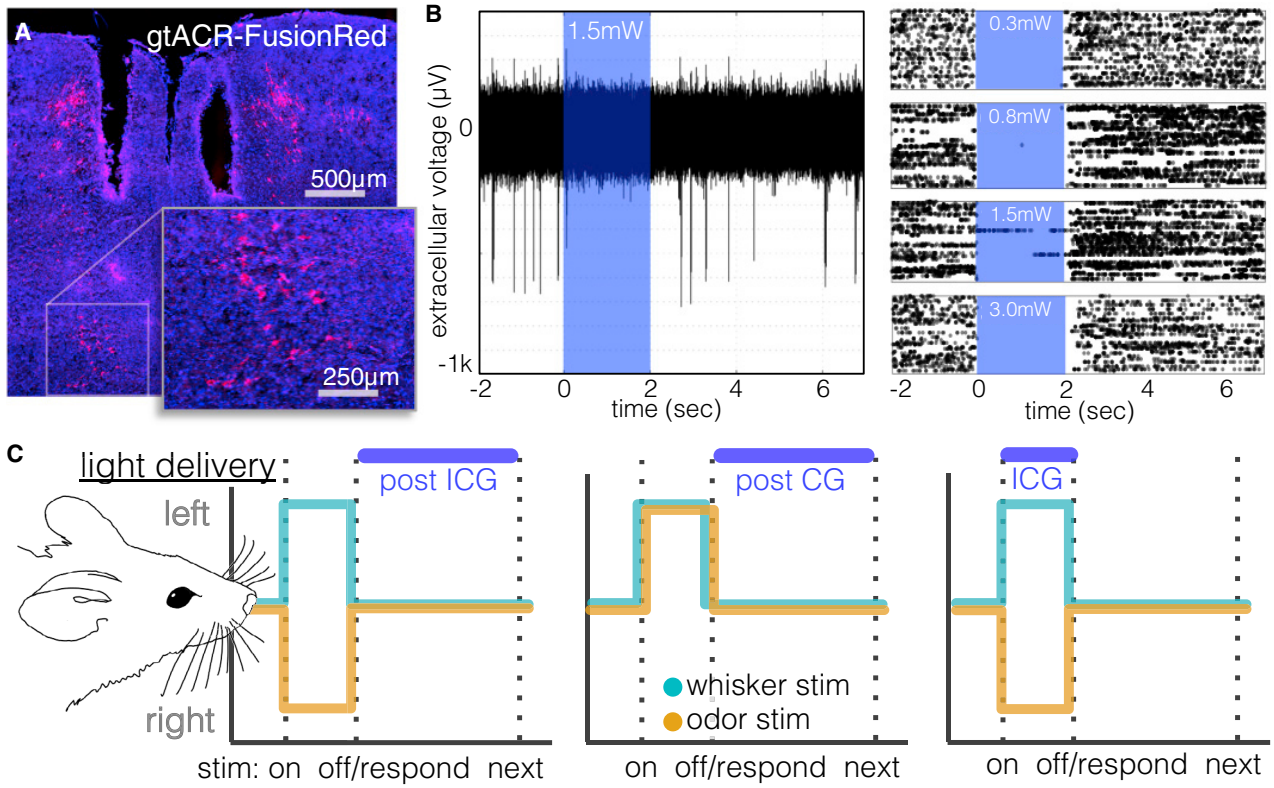

(legend on next page)

the ITI. PFC(L6)-MDT neurons showed greater *response* and *outcome* selectivity than either PFC(5)-MDT or PFC-VMS neurons and exhibited the same within-population spatial gradient seen in PFC(L5)-MDT and PFC-VMS neurons (Figure 7J). This finding was consistent across multiple statistical approaches that assessed the task feature selectivity of projection neurons as a function of their distance from the laminar surface (Figure S8). Together, these results reveal a potential source of explanatory variance for the functional heterogeneity seen in PFC neurons during set-shifting. These neurons form a topological gradient, with deeper neurons exhibiting more trial responsiveness and stronger selectivity for trial *response* and *outcome*, potentially driven by differences in their afferent connectivity profiles and in particular by differential innervation by the caudo-ventral ACC.

DISCUSSION

We began this study with the aim of more clearly resolving the circuit-level mechanisms by which prefrontal activity uses attentional sets to provide context-dependent modulation of sensorimotor processing in set-shifting tasks. The attentional set model of prefrontal involvement in cognitive flexibility, built upon decades of influential literature with thousands of citations, frames the PFC as a mediator of top-down cognitive control, which, in the context of an attentional set-shifting task, would facilitate the filtering of multimodal sensory inputs and the biasing of corresponding motor responses in accordance with context-dependent task rules. Instead, what we present is a very different model for PFC involvement in set-shifting. Rather than modulating attention in real time, PFC output neurons serve to integrate and maintain representations of recent behaviors and their consequences.

While some prior pharmacological silencing studies found that PFC activity is critical for recall, but not acquisition, of rule switching, and that PFC activity was not critical for rule switches once the rules became familiar (Rich and Shapiro, 2007), those experiments were performed in spatial tasks with changing navigation rules, which may not explicitly engage attention or suppression of irrelevant sensory cues in the same way that a cross-modal, set-shifting task does. This task difference may account for the result of the muscimol experiment in the present study, which *does* find PFC activity to be necessary for switch acquisition, as well as for continued performance of rule shifts after overtraining.

We note that the timing of rule shifts, triggered by criterion performance, means that anticipation of these rule shifts cannot be ruled out. However, such a strategy would necessarily involve acquisition of the new rule as a predicate for anticipation of the change, and it would therefore not eliminate the requirement for any of the key cognitive components of the task. Moreover, the evidence of rule-guided performance (Figure 1F) and the failure of animals to immediately abandon the previous rule following a rule shift (Figure 1G) argue against such a confound. We also note that while the training sequence used to expose animals to multiple task rules and stimulus exemplars is based on standard protocols that have been well validated by earlier set-shifting studies (Birrell and Brown, 2000; Bissonette et al., 2008; Tait et al., 2014), we did not specifically test the effect of each training step on the physiology of behavioral strategy used in the final task. Nevertheless, the essential cognitive requirements of the task, as well as the performance data analyzed both with and without perturbation (Figures 1C and 1G), strongly support the conclusion that the protocol achieves comparable results and engages the same cognitive strategy as the protocols on which this task is based.

The finding of retrospective and persistent representation of *response* and *outcome* signals, modulated by the demands of the task, is not without precedent. For example, Sul et al. (2010) found that the behavioral response in a two-armed bandit task was not represented in PFC activity in advance of the choice, but this was in an explicit test of reinforcement learning and choice valuation. The attentional set model of PFC involvement in set-shifting predicts that representations of *rule*, *whisker/odor stimuli*, and corresponding *response* should be activated during decision-making in order to modulate motor responses in downstream structures, such as striatum, thalamus, and periaqueduct gray matter.

Responsibility for modulating attention, possibly by active suppression of irrelevant stimuli, may be borne by regions with known involvement in multisensory integration—it was this hypothesis that led us to inhibit PPC activity during

Figure 6. Set-shifting performance requires PFC-VMS and PFC-MDT activity following rule-informative trials

(A) Cre-mediated expression of gtACR-FusionRed in PFC-VMS neurons and fiber tracks from chronically implanted bilateral optical fibers (fixed tissue, DAPI in blue).

(B) Electrophysiological demonstration of gtACR-mediated silencing. Left: a trace of spontaneous activity (7 s), with a 2 s light epoch interposed (1.5 mW, 470 nm light, 200 μm fiber, PFC; see STAR Methods). Right: rasters of 50 sweeps for each of four light intensities: 0.3 (top), 0.8, 1.5, and 3.0 mW (bottom).

(C) Schematic diagram of light delivery conditions. Light was delivered during the inter-trial interval following incongruent trials, following congruent trials, or during incongruent trials.

(D) Effect of light stimulation following incongruent trials on incongruent trial performance (fraction of trials correct). Left: viral control animals (tdTomato expressed in PFC); second from left: animals with pan-neuronal expression of stgtACR2 in PFC; third from left: animals with stgtACR2 expressed in PFC-VMS projection neurons. Right: animals with stgtACR2 expressed in PFC-MDT projection neurons. N = 13, 16, 17, 18 resp. Sign rank p = 0.4, 0.0005, 0.007, 0.01, resp.

(E) Effect of light stimulation during ITIs following incongruent trials on *congruent* trial performance (proportion of trials correct). Left to right: as in (A). N = 13, 16, 17, 18, resp. Sign rank p = 0.9, 0.5, 0.9, 0.07, resp.

(F) Effect of light stimulation during ITIs following congruent trials on incongruent trial performance. N = 18, 18, resp. Sign rank p = 0.1, 0.1, resp.

(G) Effect of light stimulation during trials (stimulus presentation + response window) on incongruent trial performance. N = 10 and 10, resp. Sign rank p = 0.4 and 0.4, resp. Right: effect of light delivered to posterior parietal cortex (PPC) during incongruent trials on incongruent trial performance (N = 9 animals, rank sum p = 0.02, opsin-negative control group, N = 8 animals, p = 0.74).

Please cite this article in press as: Spellman et al., Prefrontal deep projection neurons enable cognitive flexibility via persistent feedback monitoring, Cell (2021), https://doi.org/10.1016/j.cell.2021.03.047

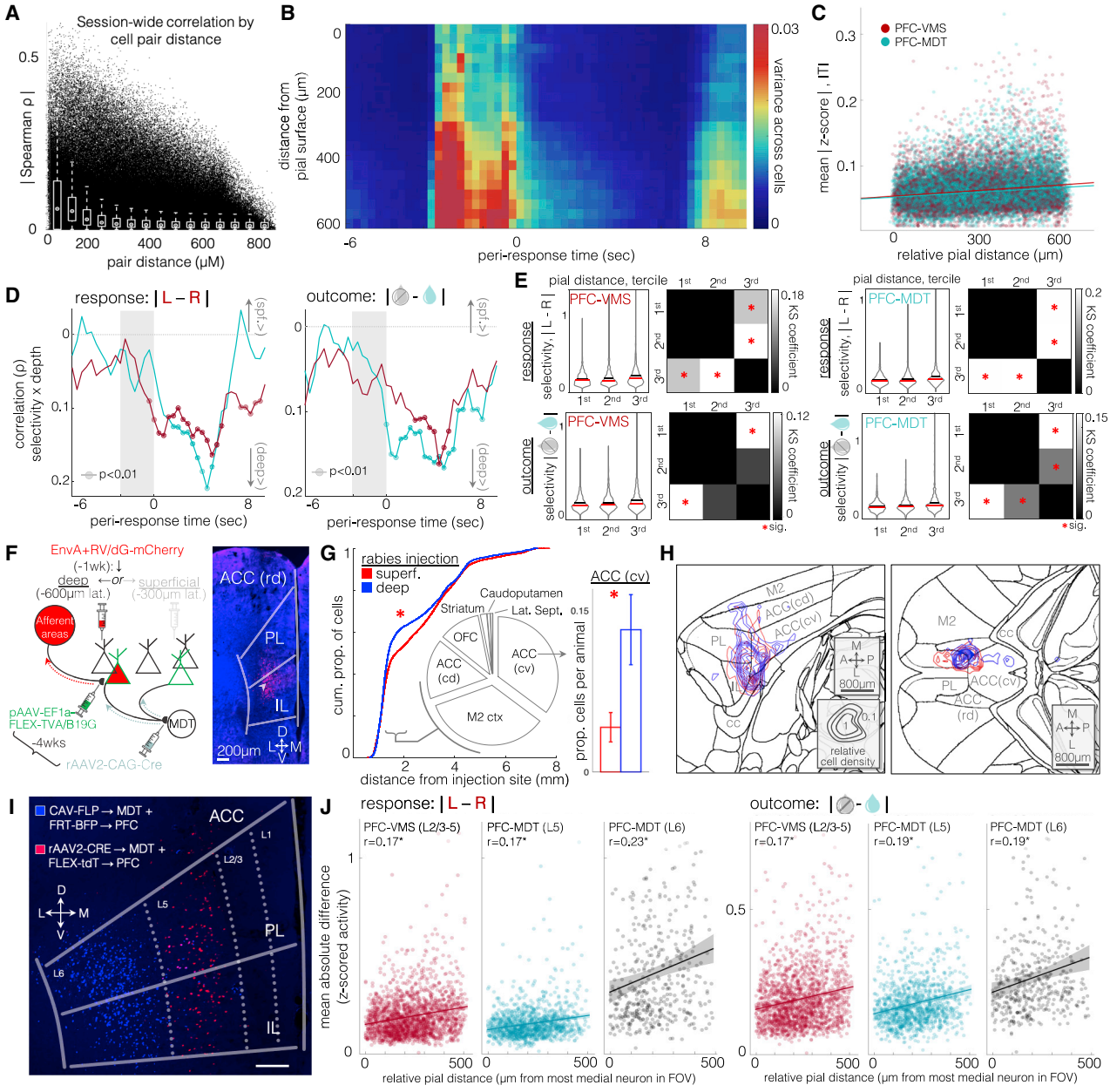

Figure 7. Post-trial feedback-related activity in projection populations is organized by a common topological gradient

(A) Spatial distance of all simultaneously recorded cell pairs versus temporal correlation. Correlations are partial correlations, controlling for changes in putative neuropil (temporal profile background component from CNMF-E source extraction algorithm). Spearman R for distance versus partial correlation is −0.25, p = 0 for N = 1,562,607 pairs from 4,740 cells in 21 animals. White plots are boxplots for 60 μm bins.

(B) Cross-neuron variance of trial-averaged activity, over trial-aligned time points and relative distance from pial surface. Warmer colors correspond with higher variance per spatiotemporal bin. Units are means of Z scored activity. Same cells as in (A).

(C) Time-averaged data from (B), broken out by neuron and by projection cell type. Correlation of absolute values of Z scored activity with relative pial distance during ITI for PFC-VMS and PFC-MDT neurons. PFC-MDT Spearman R = 0.16, p = 8×10^{-79}, 1,155 neurons, 9 animals; PFC-VMS Spearman R = 0.12, p = 3×10^{-52}, N = 1,770 neurons, 8 animals.

(D) Correlations of feature selectivity (mean absolute difference in Z scored activity between conditions) with pial distance at trial-aligned time points. Left: *response* selectivity; right: *outcome* selectivity. Circles: Spearman R < 0.01. PFC-VMS in red, PFC-MDT in green (same units as in D). Note: y axis is inverted so that "deep>" values appear on the bottom.

(E) Distributions of cell feature selectivity for *response* and *outcome* during ITI for PFC-VMS and PFC-MDT populations, binned by tercile of relative pial distance. Top row, *response* selectivity; bottom row, *outcome* selectivity; left column, PFC-VMS neurons; right column, PFC-MDT neurons. Red cross-bars are medians;

(legend continued on next page)

stimulus presentation. This perturbation did interfere with performance on ICG, but not CG, trials, lending support to the hypothesis.

Future work will seek to elucidate potential neuromodulatory and plasticity-related mechanisms behind these signals. Given the high density of input from the cholinergic nuclei of the basal forebrain that synapse on to these projection neurons (Figure S6B), and the established relationship between the central acetylcholine neuromodulatory system and attention-mediated behavior (Ljubojevic et al., 2014; Proulx et al., 2014), the possibility that acetylcholine plays a key role in mediating these feedback-monitoring signals remains strong.

Limitations of study

It is important to note also that the enhanced task responsiveness of deeply situated neurons may result from physiological mechanisms other than differential long-range inputs. Such correlates, which may include differential expression of neuromodulatory receptors, may provide a causal link between laminar position and task responsiveness and will be investigated in future work. Moreover, caution must be used in extending conclusions from rodent to primate cognition models, particularly in cases where, as in this study, the functional homology of the circuitry in question has itself been the subject of substantial debate.

STAR★METHODS

Detailed methods are provided in the online version of this paper and include the following:

- KEY RESOURCES TABLE
- RESOURCE AVAILABILITY
  - Lead contact
  - Materials availability
  - Data and code availability
- EXPERIMENTAL MODEL AND SUBJECT DETAILS
- METHOD DETAILS
  - Surgery
  - Viral Transduction
  - Muscimol silencing
  - Optogenetic implantation and stimulation
  - 2-photon imaging
  - Image processing
  - Behavioral Training and Testing Protocols
  - Training on discrimination/shifting tasks
  - Fixed tissue processing and imaging
  - Rabies tracing
  - Fluorescent axon tracing
  - Processing rabies and fluorescent axon images
  - Electrophysiological Recordings

black cross-bars are means. Binned spatial depths were tested for significant differences using a Kolmogorov-Smirnov (KS) fit test. For trial *outcome* selectivity across spatial depth, the KS chi-square for PFC-MDT neurons was 23.09, $p = 4 \times 10^{-5}$; for PFC-VMS neurons, chi-square was 19.3, p = 0.0002. For *response* selectivity across spatial depth, KS chi-square for PFC-MDT neurons was 30.2, $p = 1 \times 10^{-6}$; for PFC-VMS neurons, chi-square was 36.54, $p = 6 \times 10^{-8}$. Checkered plots are coefficients from post hoc two-sample KS tests, comparing distribution similarity across all pairs of terciles. Red asterisks are comparisons with Bonferroni-corrected significance.

(F) Left: schematic diagram of G-deleted rabies tracing experiment (see STAR Methods). Right: example coronal photomicrograph (AP +1.7 mm) of rabies-mCherry-labeled cells at a deep injection site (white arrow). N = 45,421 cells from 22 animals, 13 deep, 9 superficial injections. Starter cells were PFC-VMS (N = 6 injections) and PFC-MDT (N = 16 injections). Two-way GLM revealed no significant differences in the number of cells labeled according to projection cell type (t = 1, p = 0.3) or injection depth (t = 1.1, p = 0.3).

(G) KS comparison of cell density distributions by distance from injection site. Traces are cumulative density of cells labeled by deep (blue) and superficial (red) injections ($KS\ p = 2.07 \times 10^{-26}$, N = 9,752 and 4,755 cells from superficial and deep injections in 9 and 13 animals, respectively). The regions immediately surrounding the injection site (PL, prelimbic; IL, infralimbic; and rostral ACC, anterior cingulate cortex) were excluded, as they were likely to contain primarily starter cells. The largest difference in labeled cell density between deep and superficial injections was observed in the range of 1–2 mm distance from the injection site. We therefore compared counts in all regions containing labeled cells within this range of distances (pie chart inset). Labeled cells in this range were most dense in caudo-ventral ACC (35%), secondary motor cortex (34%), caudo-dorsal ACC (16%), orbitofrontal cortex (combined medial/lateral, 11%), striatum (2%), and caudoputamen and lateral septum (<1%). Only the caudo-ventral ACC showed a significant difference in cell count by injection depth across animals, with deep injections resulting in a higher proportion of cells in caudo-ventral (cv)-ACC than superficial injections (0.13 ± 0.03 versus 0.04 ± 0.01 of total per animal, t = 2.2, p = 0.04).

(H) Cell density contour plots for sagittal (left) and horizontal (right) cross sections through the regions surrounding ACC. Concentric contours show summed density pooled across all animals (blue, deep-injection animals; red, superficial-injection animals), normalized within the cross section shown (a.u.). Higher cv-ACC density in deep-injected neurons is shown in both orientations. Relatively higher density in M2 cortex in superficial-injection animals did not meet significance.

(I) Labeled subpopulations of PFC-MDT cells with selective tropism for rAAV2 (predominantly located in layer 5, hereafter referred to as PFC(L5)-MDT neurons) and CAV (predominantly located in layer 6, hereafter PFC(L6)-MDT neurons). Dual labeling was achieved by co-injecting a viral mixture of rAAV2-Cre and CAV2-FLP in MDT and a second viral mixture of FLEX-tdT and FRT-BFP in PFC.

(J) Pial depth and feature selectivity for the three projection subtypes. Left: Kruskal-Wallis ANOVA of cell selectivity for *response* selectivity across cell types: chi-square statistic = 440, $p = 2 \times 10^{-96}$. Post hoc GLM testing of cell type by pial distance showed significant group differences between PFC-VMS versus PFC(L6)-MDT (t = 3.4, p = 0.0007) and for PFC(L5)-MDT versus PFC(L6)-MDT (t = 3.9, p = 0.0001), but not for PFC-VMS versus PFC(L5)-MDT (t = 1.0, p = 0.3). Post hoc testing of within-group effect of pial distance on cell selectivity for *response* and trial *outcome* revealed parallel effects (no cell-type-by-pial-distance interaction effects) for all three groups. Spearman R for pial distance by *response* selectivity was significant for PFC-VMS ($r = 0.17$, $p = 1.9 \times 10^{-13}$), PFC(L5)-MDT ($r = 0.17$, $p = 6.6 \times 10^{-9}$), and PFC(L6)-MDT ($r = 0.23$, $p = 1.8 \times 10^{-6}$). Right: Kruskal-Wallis non-parametric ANOVA of cell selectivity for trial *outcome* (mean absolute difference in Z scored activity between correct and incorrect trials during the subsequent inter-trial interval) across cell types: chi-square statistic = 134, $p = 1 \times 10^{-30}$. Post hoc GLM testing of cell type by pial distance, however, showed no group differences between PFC-VMS versus PFC(L5)-MDT (t = 0.5, p = 0.6), between PFC-VMS and PFC(L6)-MDT (t = 1.25, p = 0.2), or between PFC(L5)-MDT and PFC(L6)-MDT (t = 1.6, p = 0.1). Spearman R for pial distance by trial *outcome* selectivity was also significant for each group: PFC-VMS ($r = 0.17$, $p = 1.4 \times 10^{-13}$), PFC(L5)-MDT ($r = 0.19$, $p = 8.1 \times 10^{-11}$), and PFC(L6)-MDT ($r = 0.19$, $p = 8.3 \times 10^{-5}$). PFC-VMS: N = 1,155 cells from 8 animals; PFC(L5)-MDT: N = 1,770 cells from 9 animals; PFC(L6)-MDT: N = 430 cells from 8 animals.

- QUANTIFICATION AND STATISTICAL ANALYSIS
  - Tensor component analysis (TCA)
  - Linear decoding with SVM classifiers
  - Principal components analysis (PCA)
  - General Linear Model
  - Euclidean distance and vector angles

SUPPLEMENTAL INFORMATION

Supplemental information can be found online at https://doi.org/10.1016/j.cell.2021.03.047.

ACKNOWLEDGMENTS

T.S. is supported by NIH (1K99MH117271), the Brain and Behavior Research Institute, and the Leon Levy Foundation. C.L. is supported by NIH (R01 MH109685, MH118451, MH123154) and by the Rita Allen Foundation, Hope for Depression Research Foundation, Pritzker Neuropsychiatric Disorders Research Foundation, and the Foundation for OCD Research. The authors thank S. Fusi, F. Stefanini, and L. Grosenick for consultation on the planning and implementation of data analyses.

AUTHOR CONTRIBUTIONS

C.L. and T.S. designed the behavioral task and planned the study. T.S. and M.S. performed the injection and implantation surgeries and gathered the behavioral data. T.S. and M.S. performed the neural recordings. T.S. analyzed the behavioral and neural data. J.K. performed the TCA analysis. G.M.-N. assisted with the EnvA-G-deleted rabies experiment. T.S. and C.L. wrote and edited the manuscript.

DECLARATION OF INTERESTS

The authors declare no competing interests.

Received: January 5, 2020
Revised: February 16, 2021
Accepted: March 23, 2021
Published: April 15, 2021

REFERENCES

Adesnik, H., and Naka, A. (2018). Cracking the Function of Layers in the Sensory Cortex. Neuron *100*, 1028–1043.

Akrami, A., Kopec, C., Diamond, M., and Brody, C. (2018). Posterior parietal cortex represents sensory history and mediates its effects on behaviour. Nature *554*, 368–372.

Andermann, M.L., Gilfoy, N.B., Goldey, G.J., Sachdev, R.N., Wölfel, M., McCormick, D.A., Reid, R.C., and Levene, M.J. (2013). Chronic cellular imaging of entire cortical columns in awake mice using microprisms. Neuron *80*, 900–913.

Aoki, S., Liu, A.W., Zucca, A., Zucca, S., and Wickens, J.R. (2015). Role of striatal cholinergic interneurons in set-shifting in the rat. J. Neurosci. *35*, 9424–9431.

Bari, B.A., Grossman, C.D., Lubin, E.E., Rajagopalan, A.E., Cressy, J.I., and Cohen, J.Y. (2019). Stable Representations of Decision Variables for Flexible Behavior. Neuron *103*, 922–933.e7.

Bernacchia, A., Seo, H., Lee, D., and Wang, X. (2011). A reservoir of time constants for memory traces in cortical neurons. Nat. Neurosci. *14*, 366–372.

Biró, S., Lasztóczi, B., and Klausberger, T. (2019). A visual two-choice rule-switch task for head-fixed mice. Front. Behav. Neurosci. *13*, 119.

Birrell, J.M., and Brown, V.J. (2000). Medial frontal cortex mediates perceptual attentional set shifting in the rat. J. Neurosci. *20*, 4320–4324.

Bissonette, G.B., and Roesch, M.R. (2015). Neural correlates of rules and conflict in medial prefrontal cortex during decision and feedback epochs. Front. Behav. Neurosci. *9*, 266.

Bissonette, G.B., Martins, G.J., Franz, T.M., Harper, E.S., Schoenbaum, G., and Powell, E.M. (2008). Double dissociation of the effects of medial and orbital prefrontal cortical lesions on attentional and affective shifts in mice. J. Neurosci. *28*, 11124–11130.

Bissonette, G.B., Powell, E.M., and Roesch, M.R. (2013). Neural structures underlying set-shifting: roles of medial prefrontal cortex and anterior cingulate cortex. Behav. Brain Res. *250*, 91–101.

Block, A.E., Dhanji, H., Thompson-Tardif, S.F., and Floresco, S.B. (2007). Thalamic-prefrontal cortical-ventral striatal circuitry mediates dissociable components of strategy set shifting. Cereb. Cortex *17*, 1625–1636.

Bortolato, B., Miskowiak, K.W., Köhler, C.A., Maes, M., Fernandes, B.S., Berk, M., and Carvalho, A.F. (2016). Cognitive remission: a novel objective for the treatment of major depression? BMC Med. *14*, 9.

Brigman, J.L., Bussey, T.J., Saksida, L.M., and Rothblat, L.A. (2005). Discrimination of multidimensional visual stimuli by mice: intra- and extradimensional shifts. Behav. Neurosci. *119*, 839–842.

Brinkman, B., and Charikar, M. (2005). On the impossibility of Dimension Reduction. J. Assoc. Comput. Mach. *52*, 766–788.

Campbell, B., Nabel, E., Murdock, M., Lao-Peregrin, C., Tsoulfas, P., Blackmore, M., Lee, F., Liston, C., Morishita, H., and Petsko, G. (2020). mGreenLantern: a bright monomeric fluorescent protein with rapid expression and cell filling properties for neuronal imaging. Proc. Natl. Acad. Sci. USA *117*, 30710–30721.

Ceaser, A.E., Goldberg, T.E., Egan, M.F., McMahon, R.P., Weinberger, D.R., and Gold, J.M. (2008). Set-shifting ability and schizophrenia: a marker of clinical illness or an intermediate phenotype? Biol. Psychiatry *64*, 782–788.

Chen, T., Wardill, T., Sun, Y., Pulver, S., Renninger, S., Baohan, A., Schreiter, E., Kerr, R., Orger, M., Jayaraman, V., et al. (2013). Ultrasensitive fluorescent proteins for imaging neuronal activity. Nature *499*, 295–300.

Christianini, N., and Shawe-Taylor, J. (2000). An Introduction to Support Vector Machines and Other Kernel-Based Learning Methods (Cambridge University Press).

Collins, D.P., Anastasiades, P.G., Marlin, J.J., and Carter, A.G. (2018). Reciprocal Circuits Linking the Prefrontal Cortex with Dorsal and Ventral Thalamic Nuclei. Neuron *98*, 366–379.e4.

Corbetta, M., and Shulman, G. (2002). Control of goal-directed and stimulus-driven attention in the brain. Nat. Rev. Neurosci. *3*, 201–215.

Crowe, S.E., and Ellis-Davies, G.C. (2014). Longitudinal in vivo two-photon fluorescence imaging. J. Comp. Neurol. *522*, 1708–1727.

Denk, W., Strickler, J.H., and Webb, W.W. (1990). Two-photon laser scanning fluorescence microscopy. Science *248*, 73–76.

Desimone, R., and Duncan, J. (1995). Neural mechanisms of selective visual attention. Annu. Rev. Neurosci. *18*, 193–222.

Disner, S.G., Beevers, C.G., Haigh, E.A.P., and Beck, A.T. (2011). Neural mechanisms of the cognitive model of depression. Nat. Rev. Neurosci. *12*, 467–477.

Durstewitz, D., Vittoz, N.M., Floresco, S.B., and Seamans, J.K. (2010). Abrupt transitions between prefrontal neural ensemble states accompany behavioral transitions during rule learning. Neuron *66*, 438–448.

Ellwood, I.T., Patel, T., Wadia, V., Lee, A.T., Liptak, A.T., Bender, K.J., and Sohal, V.S. (2017). Tonic or Phasic Stimulation of Dopaminergic Projections to Prefrontal Cortex Causes Mice to Maintain or Deviate from Previously Learned Behavioral Strategies. J. Neurosci. *37*, 8315–8329.

Floresco, S.B., Ghods-Sharifi, S., Vexelman, C., and Magyar, O. (2006). Dissociable roles for the nucleus accumbens core and shell in regulating set shifting. J. Neurosci. *26*, 2449–2457.

Fox, M., Barense, M., and Baxter, M. (2003). Perceptual attentional set-shifting is impaired in rats with neurotoxic lesions of posterior parietal cortex. J. Neurosci. *23*, 676–681.

Friedrich, J., Zhou, P., and Paninski, L. (2017). Fast online deconvolution of calcium imaging data. PLoS Comput. Biol. *13*, e1005423.

Gonda, X., Pompili, M., Serafini, G., Carvalho, A.F., Rihmer, Z., and Dome, P. (2015). The role of cognitive dysfunction in the symptoms and remission from depression. Ann. Gen. Psychiatry *14*, 27.

Halleland, H.B., Haavik, J., and Lundervold, A.J. (2012). Set-shifting in adults with ADHD. J. Int. Neuropsychol. Soc. *18*, 728–737.

Harris, K.D., and Shepherd, G.M. (2015). The neocortical circuit: themes and variations. Nat. Neurosci. *18*, 170–181.

Harvey, P.D., Green, M.F., Keefe, R.S., and Velligan, D.I. (2004). Cognitive functioning in schizophrenia: a consensus statement on its role in the definition and evaluation of effective treatments for the illness. J. Clin. Psychiatry *65*, 361–372.

Heisler, J.M., Morales, J., Donegan, J.J., Jett, J.D., Redus, L., and O'Connor, J.C. (2015). The Attentional Set Shifting Task: A Measure of Cognitive Flexibility in Mice. J. Vis. Exp. *96*, 51944.

Hyman, J.M., Ma, L., Balaguer-Ballester, E., Durstewitz, D., and Seamans, J.K. (2012). Contextual encoding by ensembles of medial prefrontal cortex neurons. Proc. Natl. Acad. Sci. USA *109*, 5086–5091.

Hnasko, T., Perez, F., Scouras, A., Stoll, E., Gale, S., Luquet, S., Phillips, P., Kremer, E., and Palmiter, R. (2006). Cre recombinase-mediated restoration of nigrostriatal dopamine in dopamine-deficient mice reverses hypophagia and bradykinesia. Proc Natl Acad Sci *103*, 8858–8863. https://doi.org/10.1073/pnas.0603081103.

Hyman, J., Holroyd, C., and Seamans, J. (2017). A Novel Neural Prediction Error Found in Anterior Cingulate Cortex Ensembles. Neuron *95*, 447–456.e3.

Jazbec, S., Pantelis, C., Robbins, T., Weickert, T., Weinberger, D.R., and Goldberg, T.E. (2007). Intra-dimensional/extra-dimensional set-shifting performance in schizophrenia: impact of distractors. Schizophr. Res. *89*, 339–349.

Kato, S., Fukabori, R., Nishizawa, K., Okada, K., Yoshioka, N., Sugawara, M., Maejima, Y., Shimomura, K., Okamoto, M., Eifuku, S., et al. (2018). Action Selection and Flexible Switching Controlled by the Intralaminar Thalamic Neurons. Cell Rep. *22*, 2370–2382.

Kim, C., Cilles, S.E., Johnson, N.F., and Gold, B.T. (2012). Domain general and domain preferential brain regions associated with different types of task switching: a meta-analysis. Hum. Brain Mapp. *33*, 130–142.

Ljubojevic, V., Luu, P., and De Rosa, E. (2014). Cholinergic contributions to supramodal attentional processes in rats. J. Neurosci. *34*, 2264–2275.

Low, R.J., Gu, Y., and Tank, D.W. (2014). Cellular resolution optical access to brain regions in fissures: imaging medial prefrontal cortex and grid cells in entorhinal cortex. Proc. Natl. Acad. Sci. USA *111*, 18739–18744.

Lui, J., Nguyen, N., Grutzner, S., Darmanis, S., Peixoto, D., Wagner, M., Allen, W., Kebschull, J., Richman, E., Ren, J., et al. (2021). Differential encoding in prefrontal cortex projection neuron classes across cognitive tasks. Cell *184*, 489–506.e26.

MacDonald, A.W., 3rd, Cohen, J.D., Stenger, V.A., and Carter, C.S. (2000). Dissociating the role of the dorsolateral prefrontal and anterior cingulate cortex in cognitive control. Science *288*, 1835–1838.

Mahn, M., Gibor, L., Patil, P., Cohen-Kashi Malina, K., Oring, S., Printz, Y., Levy, R., Lampl, I., and Yizhar, O. (2018). High-efficiency optogenetic silencing with soma-targeted anion-conducting channelrhodopsins. Nat. Commun. *9*, 4125.

Mante, V., Sussillo, D., Shenoy, K., and Newsome, W. (2013). Context-dependent computation by recurrent dynamics in prefrontal cortex. Nature *503*, 78–84.

Marshel, J., Kim, Y., Machado, T., Quirin, S., Benson, B., Kadmon, J., Raja, C., Chibukhchyan, A., Ramakrishnan, C., Inoue, M., et al. (2019). Cortical layer-specific critical dynamics triggering perception. Science *365*, eaaw5202.

Marton, T.F., Seifikar, H., Luongo, F.J., Lee, A.T., and Sohal, V.S. (2018). Roles of Prefrontal Cortex and Mediodorsal Thalamus in Task Engagement and Behavioral Flexibility. J. Neurosci. *38*, 2569–2578.

Meyers, E.M., Freedman, D.J., Kreiman, G., Miller, E.K., and Poggio, T. (2008). Dynamic population coding of category information in inferior temporal and prefrontal cortex. J. Neurophysiol. *100*, 1407–1419.

Miller, E.K., and Cohen, J.D. (2001). An integrative theory of prefrontal cortex function. Annu. Rev. Neurosci. *24*, 167–202.

Milner, B. (1963). Effects of different brain lesions on card sorting: The role of the frontal lobes. Arch. Neurol. *9*, 100–110.

Murphy, F.C., Michael, A., and Sahakian, B.J. (2012). Emotion modulates cognitive flexibility in patients with major depression. Psychol. Med. *42*, 1373–1382.

Nakai, J., Ohkura, M., and Imoto, K. (2001). A high signal-to-noise Ca(2+) probe composed of a single green fluorescent protein. Nat. Biotechnol. *19*, 137–141.

Nakayama, H., Ibañez-Tallon, I., and Heintz, N. (2018). Cell-type-specific contributions of medial prefrontal neurons to flexible behaviors. J. Neurosci. *38*, 4490–4504.

Otis, J.M., Namboodiri, V.M.K., Matan, A.M., Voets, E.S., Mohorn, E.P., Kosyk, O., McHenry, J.A., Robinson, J.E., Resendez, S.L., Rossi, M.A., and Stuber, G.D. (2017). Prefrontal cortex output circuits guide reward seeking through divergent cue encoding. Nature *543*, 103–107.

Pnevmatikakis, E.A., and Giovannucci, A. (2017). NoRMCorre: An online algorithm for piecewise rigid motion correction of calcium imaging data. J. Neurosci. Methods *291*, 83–94.

Pnevmatikakis, E.A., Soudry, D., Gao, Y., Machado, T.A., Merel, J., Pfau, D., Reardon, T., Mu, Y., Lacefield, C., Yang, W., et al. (2016). Simultaneous Denoising, Deconvolution, and Demixing of Calcium Imaging Data. Neuron *89*, 285–299.

Prado, V., Janickova, H., Al-Onaizi, M., and Prado, M. (2017). Cholinergic circuits in cognitive flexibility. Neuroscience *345*, 130–141.

Proulx, E., Piva, M., Tian, M.K., Bailey, C.D., and Lambe, E.K. (2014). Nicotinic acetylcholine receptors in attention circuitry: the role of layer VI neurons of prefrontal cortex. Cell. Mol. Life Sci. *71*, 1225–1244.

Rich, E., and Shapiro, M. (2007). Prelimbic/Infralimbic Inactivation Impairs Memory for Multiple Task Switches, But Not Flexible Selection of Familiar Tasks. J. Neurosci. *27*, 4747–4755.

Rich, E.L., and Shapiro, M. (2009). Rat prefrontal cortical neurons selectively code strategy switches. J. Neurosci. *29*, 7208–7219.

Rigotti, M., Barak, O., Warden, M.R., Wang, X.J., Daw, N.D., Miller, E.K., and Fusi, S. (2013). The importance of mixed selectivity in complex cognitive tasks. Nature *497*, 585–590.

Rodgers, C.C., and DeWeese, M.R. (2014). Neural correlates of task switching in prefrontal cortex and primary auditory cortex in a novel stimulus selection task for rodents. Neuron *82*, 1157–1170.

Schmitt, L., Wimmer, R., Nakajima, M., Happ, M., MofakHam, S., and Halassa, M. (2017). Thalamic amplification of cortical connectivity sustains attentional control. Nature *545*, 219–223.

Schmitzer-Torbert, N., Jackson, J., Henze, D., Harris, K., and Redish, A.D. (2005). Quantitative measures of cluster quality for use in extracellular recordings. Neuroscience *131*, 1–11.

Senzai, Y., Fernandez-Ruiz, A., and Buzsaki, G. (2019). Layer-Specific Physiological Features and Interlaminar Interactions in the Primary Visual Cortex of the Mouse. Neuron *101*, P500-513.E5.

Shamash, P., Carandini, M., Harris, K., and Steinmetz, N. (2018). A tool for analyzing electrode tracks from slice histology. BioRxiv. https://doi.org/10.1101/447995.

Sharif, F., Tayebi, B., Buzsaki, G., Royer, S., and Fernandez-Ruiz, A. (2021). Subcircuits of Deep and Superficial CA1 Place Cells Support Efficient Spatial Coding across Heterogeneous Environments. Neuron *109*, 363–376.e6.

Sheintuch, L., Rubin, A., Brande-Eilat, N., Geva, N., Sadeh, N., Pinchasof, O., and Ziv, Y. (2017). Tracking the Same Neurons across Multiple Days in Ca^{2+} Imaging Data. Cell Rep. *21*, 1102–1115.

Siniscalchi, M., Phoumthipphavong, V., Ali, F., Lozano, M., and Kwan, A. (2016). Fast and slow transitions in frontal ensemble activity during flexible sensorimotor behavior. Nat. Neurosci. *19*, 1234–1242.

Siniscalchi, M., Wang, H., and Kwan, A. (2019).). Enhanced Population Coding for Rewarded Choices in the Medial Frontal Cortex of the Mouse. Cereb. Cortex *29*, 4090–4106.

Smith, M.A., and Kohn, A. (2008). Spatial and temporal scales of neuronal correlation in primary visual cortex. J. Neurosci. *28*, 12591–12603.

Soudais, C., Laplace-Builhe, C., Kissa, K., and Kremer, E.J. (2001). Preferential transduction of neurons by canine adenovirus vectors and their efficient retrograde transport in vivo. FASEB J. *15*, 2283–2285.

Starkweather, C., Gershman, S., and Uchida, N. (2018). The Medial Prefrontal Cortex Shapes Dopamine Reward Prediction Errors under State Uncertainty. Neuron *98*, 616–629.e6.

Stringer, C., and Pachitariu, M. (2019). Computational processing of neural recordings from calcium imaging data. Curr. Opin. Neurobiol. *55*, 22–31.

Sul, J., Kim, H., Huh, N., Lee, D., and Jung, M. (2010). Distinct roles of rodent orbitofrontal and medial prefrontal cortex in decision making. Neuron *66*, 449–460.

Tait, D.S., Chase, E.A., and Brown, V.J. (2014). Attentional set-shifting in rodents: a review of behavioural methods and pharmacological results. Curr. Pharm. Des. *20*, 5046–5059.

Tervo, D., Hwang, B., Viswanathan, S., Gaj, T., Lavzin, M., Ritola, K., Lindo, S., Michael, S., Kuleshova, E., Ojala, D., et al. (2016). A Designer AAV Variant Permits Efficient Retrograde Access to Projection Neurons. Neuron *92*, 372–382.

Turner, J., Parrish, J., Hughes, L., Toth, L., and Caspary, D. (2005). Hearing in Laboratory Animals: Strain Differences and Nonauditory Effects of Noise. Comp. Med. *55*, 12–23.

Wang, Q., Ding, S., Li, Y., Royall, J., Feng, D., Lesnar, P., Graddis, N., Naeemi, M., Facer, B., Ho, A., et al. (2020). The Allen Mouse Brain Common Coordinate Framework: A 3D Reference Atlas. Cell *181*, 936–953.e20.

Williams, A.H., Kim, T.H., Wang, F., Vyas, S., Ryu, S.I., Shenoy, K.V., Schnitzer, M., Kolda, T.G., and Ganguli, S. (2018). Unsupervised Discovery of Demixed, Low-Dimensional Neural Dynamics across Multiple Timescales through Tensor Component Analysis. Neuron *98*, 1099–1115.e8.

Wimmer, R., Schmidt, L., Davidson, T., Nakajima, M., Deisseroth, K., and Halassa, M. (2015). Thalamic control of sensory selection in divided attention. Nature *526*, 705–709.

Please cite this article in press as: Spellman et al., Prefrontal deep projection neurons enable cognitive flexibility via persistent feedback monitoring, Cell (2021), https://doi.org/10.1016/j.cell.2021.03.047

STAR★METHODS

KEY RESOURCES TABLE

REAGENT or RESOURCE	SOURCE	IDENTIFIER
Bacterial and virus strains		
pAAV1-Syn-FLEX-GCaMP6f-WPRE.SV40	Addgene	100833-AAV1
pAAV1-Syn-GCaMP6f-WPRE.SV40	Addgene	100837-AAV1
rAAV2(retro)-CAG-Cre-WPRE	Vector Biolabs	VB5075
rAAV2-CAG-mGreenLantern	Campbell et al., 2020	Addgene 164469
AAV9-CAG-F3/FRT-NLS-tdTomato-WPRE	Vector Biolabs	Addgene 37347
CAV2-Cre	(Hnasko et al., 2006)	https://www.pvm.cnrs.fr/
CAV2-FLP	(Hnasko et al., 2006)	https://www.pvm.cnrs.fr/
pAAV-EF1a-FLEX-TVA/B19	Addgene	26197
EnvA G-Deleted Rabies-mCherry	Salk Institute	N/A
AAV1-CAG-FLEX-tdTomato	Addgene	28306-AAV1
AAV1-hSyn-stGtACR2-FusionRed	Addgene	105677-AAV1
Chemicals, peptides, and recombinant proteins		
Muscimol	Sigma Aldrich	M1523-5MG
Fluorescent muscimol	Sigma Aldrich	M3-633-AN
Experimental models: organisms/strains		
Mouse: C57BL/6J, male	Jackson Lab	000664
Software and algorithms		
MATLAB v2019b	Mathworks	N/A
Python3	Python Software Fdn	Python.org
NoRMCorre	(Pnevmatikakis and Giovannucci, 2017)	https://github.com/flatironinstitute/NoRMCorre
CNMF-E	Pnevmatikakis et al., 2016	https://github.com/zhoupc/CNMF_E
allenCCF	Shamash et al., 2018	https://github.com/cortex-lab/allenCCF
tensortools	Williams et al., 2018	https://github.com/ahwillia/tensortools

RESOURCE AVAILABILITY

Lead contact

Further information and requests for resources and reagents should be directed to and will be fulfilled by the lead contact, Conor Liston (col2004@med.cornell.edu).

Materials availability

This study did not generate new unique reagents.

Data and code availability

Available upon request.

EXPERIMENTAL MODEL AND SUBJECT DETAILS

Male C57BL/6 mice (Jackson Labs) were used for all experiments, aged 6-10 weeks at first use. Mice were housed in a Weill Cornell Medical College facility and were maintained on a 12-hour light-dark cycle. Except when water-restricted for the purpose of behavioral training and testing, all mice were given *ad libitum* access to food and water. Littermates underwent prism or fiber implant surgeries within the same week, and mice were group-housed with littermates with the same surgery status. All procedures were approved by the Weill Cornell Medicine IACUC. Sample sizes for each experiment were determined using power analysis estimates computed in MATLAB, based on anticipated effect sizes that were estimated from previously published reports whenever they were available, and were powered to detect moderate, biologically meaningful effect sizes.

Please cite this article in press as: Spellman et al., Prefrontal deep projection neurons enable cognitive flexibility via persistent feedback monitoring, Cell (2021), https://doi.org/10.1016/j.cell.2021.03.047

METHOD DETAILS

Surgery

Animals were placed inside a flow box and anesthetized with isoflurane gas (2%) until sedated, at which point they were placed in a stereotax and maintained on 0.5% isoflurane for the duration of the surgery. Scalp hair was trimmed away, and a midline incision was made using fine surgical scissors (Fine Science Tools), exposing the skull. The periosteum was bluntly dissected away and bupivacaine (0.05 mL, 5 mg/kg) was topically applied. For prism implantation, a large rectangular craniotomy was made above left PFC, extending from 1.5mm anterior to 3.7mm anterior, and from 2.0mm lateral (left) to 0.2mm lateral (right, across midline).

A 0.5-mm burr (Fine Science Tools) and a high-speed hand dental drill (Osada) were used, taking great care not to compress brain tissue or damage the sagittal venous sinus. In the event of venous bleeding, Gelfoam (Pfizer) was applied to the dura surface to accelerate clotting. Gentle irrigation with phosphate-buffered saline (137 mM NaCl, 27 mM KCl, 10 mM phosphate buffer, VWR) was used to clear debris at regular intervals. The dura beneath the craniotomy was removed using the tip of a 26 g insulin syringe (VWR) and fine forceps (Fine Science Tools).

Chronically implanted microprisms (1.5mm X 1.5mm X 3mm; M/L,A/P,D/V), from OptoSigma (BK7 borosilicate glass with aluminum hypotenuse and silicon dioxide coating), were implanted at a depth of 2.3mm ventral to brain surface using a stereotaxic micromanipulator (Kopf). During implantation, the prism was held in place using vacuum suction via an 18G blunt needle. As in previous studies (Andermann et al., 2013; Low et al., 2014) minimal reactive gliosis was seen in the coronal imaging field, and maximum calcium-mediated fluorescence was seen 50-150 μm past the prism face; therefore imaging planes were confined to this depth.

For PFC-VMS and PFC-MDT projection targeting, an additional craniotomy was made at 1.25mm/1.25mm A/L or 1.2mm/0.35mm P/L, respectively. All head-fixed animals received custom-machined stainless steel head plates affixed to skull surface with Metabond dental cement. Head plates featured a circular central aperture centered around the imaging field (9mm I.D.), with right and left securing arms (25mm total width) that accommodated 0-80 socket screws (0.38 g in total). Sterile eye lubricant (Puralube, FischerSci) was administered to prevent corneal drying, and a microwavable heating pad (Snugglesafe) was used to maintain body temperature. Metacam (1 mg/kg, i.p.) was administered after surgery as a prophylactic analgesic.

Viral Transduction

AAV of titer exceeding 10^{12}vg/ml (Vector Biolabs, UNC Vector Core and Addgene) was used to package the plasmids. For imaging experiments, AAV1-hSyn-GCaMP6f or AAV1-hSyn-DIO-GCaMP6f (Chen et al., 2013) was targeted to PFC. Injection coordinates for PFC were 1.75mm anterior. Two parallel injection tracks were made at 0.2mm and 0.5mm lateral, and in each of these tracks, two D/V sites received infusions, at 2.0mm and 1.5mm ventral to brain surface. For rAAV2-Cre projection targeting, VMS injections were delivered at 1.25mm/1.25mm/4.7mm A/L/V, and MDT injections at 1.2mm/0.35mm/3.2mm P/L/V. Hamilton syringes and beveled 36G or 33G NanoFil needles (WPI) were used, and at each site, the needle was allowed to sit 5min to allow for tissue settling before infusion. Virus was infused at a rate of 50nL/min, for a total of 250nL per site.

For the dual labeling tracing experiment (Figure 5B), rAAV2-mGreenLantern (Campbell et al., 2020) was injected in MDT (500nL), CAV-FLP was injected in VMS (500nL), and AAV9-CAG-F3/FRT-NLS-tdTomato-WPRE was injected in PFC (500nL).

Muscimol silencing

Animals received chronically implanted 26G bilateral stainless steel guide cannulae (Plastics One), implanted at 1.75mm/0.35mm/1mm A/L/V. After undergoing the training and task transition sequence up to and including Reversal (see behavioral training protocol below), animals underwent muscimol infusion. In a familiar cage, bilateral internal infusion cannulae were inserted into the guide cannulae, protruding 0.5mm from the end of the guide cannulae, and were left for 5min to allow tissue to settle. Muscimol (1 μg/μL) or physiological saline (0.9%) was infused at a rate of 50nL/min, for a total of 0.25 μL. Five minutes after completion of the infusion, the internal cannulae were removed and the mouse immediately began behavioral testing.

Optogenetic implantation and stimulation

Bilateral fibers were implanted over PFC (Thorlabs dual fiber cannulae, 700 μm center-to-center spacing, 200 μm core) at 0.35mm lateral, 1.75 anterior, 1.2mm ventral to brain surface. In the posterior parietal cortex inhibition cohort, in order to cover the medial-lateral extent of PPC, a dual-fiber cannula (700 μm center-to-center spacing) was placed over each hemisphere, so that both right and left PPC each had two 200 μm-core fibers. The dual fiber cannulae were positioned on the brain surface with the dura intact, at a ML angle of 10° away from midline, with the medial fiber at AP −1.8mm, ML +1.0mm, and the lateral fiber at AP −1.8mm, ML +1.7mm. Light was delivered via Thorlabs M470F3 fiber-coupled LED, 1.5-3mW light power from each fiber. In the trial-concurrent stimulation condition, photoactivation was initiated at the same time as the 500ms trial-ready cue and persisted through the 2.5 s stimulus presentation epoch until either a lick terminated the trial or the 1.5 s response period expired. In the inter-trial interval stimulation conditions, photoactivation was initiated concurrently with the end of the trial (first lick within the response window or upon the conclusion of the 1.5 s response window without a lick) and persisted through the 8-10 s post-trial epoch, terminating with the onset of the subsequent trial-ready cue. In the experiment testing the effects of inhibition during the beginning of the inter-trial interval, the photoactivation was initiated concurrently with lickspout selection and persisted for 4.5 s before terminating; in the experiment testing the effects of inhibition during the end of the inter-trial interval, photoactivation was initiated beginning at

Please cite this article in press as: Spellman et al., Prefrontal deep projection neurons enable cognitive flexibility via persistent feedback monitoring, Cell (2021), https://doi.org/10.1016/j.cell.2021.03.047

4.5 s following lickspout selection, persisting for the remainder of the 8-10 s inter-trial interval. Light was delivered in alternating trial blocks, beginning with the second block of the session (no light delivered in the initial block). Sessions in which animals failed to reach criterion on the initial block were re-run until the animal reached criterion.

2-photon imaging

2-photon calcium imaging (Denk et al., 1990; Nakai et al., 2001) was performed via an Olympus 10x 0.6NA objective, with 8mm working distance. All images were acquired using a commercial two-photon laser-scanning microscope (Olympus RS) equipped with a scanning galvanometer and a Spectra-Physics Mai Tai DeepSee laser tuned to 920nm, operating at 300-500mW. Fluorescence was recorded through gallium arsenide phosphide (GaAsP) detectors using the Fluoview acquisition software (Olympus) using a green light emission bandpass filter (Semrock). Imaging sessions began by performing an isosbestic anatomical scan (810nm 2P excitation light) to aid in relocating the same sites over multiple sessions. Calcium signals were acquired at 256 × 130 pixel resolution, covering a 1500 μm X 760 μm field of view, with a μm/pixel ratio of 5.85. The scan time was 346ms, with a frame rate of 2.89Hz. All calcium imaging experiments occurred in awake mice. For analysis of SEDS sessions, sessions were concatenated using CellReg (Sheintuch et al., 2017) and non-rigid spatial transformation (see Videos S1 and S2 for examples). Neurons were modeled with a maximal centroid distance of 15 μm and a threshold correlation of 0.65. Z-scoring of deconvolved activity traces was performed prior to concatenating across sessions. SEDS neural datasets for each of 21 animals are comprised of a median of 3 sessions (2.5,4 upper, lower quartiles), 1462 trials (1034, 1667 upper, lower quartiles), and 11 set shifts (8.5, 17.5 upper, lower quartiles).

Image processing

Videos were motion-corrected using NoRMCorre (Pnevmatikakis and Giovannucci, 2017) implemented in MATLAB (Mathworks), and a constrained non-negative matrix factorization-based source extraction method was used to denoise, deconvolve and demix the videos to extract neural traces (using the extensively validated CNMF-E package (Pnevmatikakis et al., 2016) with OASIS signal deconvolution (Friedrich et al., 2017). Sources were well separated from both neighboring sources and surrounding neuropil, as assessed by performing PCA analysis of putative source and surrounding pixels over time and quantifying their isolation distances (Schmitzer-Torbert et al., 2005; Stringer and Pachitariu, 2019). The resulting traces were deconvolved calcium traces corresponding with estimated event rates, which were then z-scored over the full session to normalize. Calcium signals from sequential sessions were concatenated using non-rigid co-registration of spatial cell footprints using CellReg (Crowe and Ellis-Davies, 2014; Sheintuch et al., 2017), (see Figures S2, S3, and S4 for example traces and quality control metrics).

Behavioral Training and Testing Protocols

Animals recovered 14 days from surgery before being placed on water restriction for four days, after which they typically drank 1-1.2mL/day. Behavioral training and testing procedures were carried out 5 days per week, with each animal undergoing one session per day. Animals underwent two days of hand-feeding, in which they were handled for up to ten minutes by the experimenter while receiving water from a 1mL syringe with a rounded stainless steel gavage needle.

Habituation-1

Following two days of hand-feeding, animals underwent a *Habituation-1* session in the behavioral apparatus, which consisted of an aluminum restraint tube with dual lickspouts positioned at one end. The restraint tube was 27mm in diameter, a width calibrated to allow the animal to groom and adjust its posture during sessions but which prevented significant lateral or vertical body movement. During *Habituation-1*, lickspouts were alternately armed so that a single lick would trigger delivery of a 3uL water bolus, and the identity of the armed lickspout changed every 1-4 trials, with a 1.5 s timeout after each bolus delivery. This alternating schedule forced the animal to explore both lickspouts equally to maximize rewards. Animals would periodically venture out of the restraint tube to explore the behavior chamber, at which point the experimenter would guide them back into the tube by hand. The session terminated when the animal stopped licking for ~2min, and the animal was considered to have passed this stage when it had consumed 500 μL in a session.

Habituation-2

After passing Habituation-1, animals underwent a *Habituation-2* stage, which consisted of the same lick/dispense schedule as Habituation-1, but during which the animal was head-restrained for the first time. Here again, the animal needed to consume 500 μL to pass.

Habituation-3

After Habituation-2, animals underwent *Habituation-3*, in which lickspouts alternated every 20 lick/delivery trials, to establish left/right trial blocks. As with Habituation-1 and −2, animals were considered to have passed this stage after consuming 500 μL of water.

Shaping-1

After this, animals underwent a *Shaping-1* session, which introduced the trial structure to be used for the rest of the sessions: a 500ms white noise trial-start cue was presented, followed by a 2.5 s stimulus (whisker or odor, depending on the training sequence, which was counter-balanced across animals in the calcium imaging experiment), followed by a ≤ 1.5 s response window, during which the correct lickspout was armed. When the response rate fell to between 0.3 and 0.6 within a 10-trial moving window, reward would be dispensed regardless of whether the animal licked, in order to promote licking. Trials were blocked (20 right, 20 left), and a lick to the

incorrect side would not terminate the trial; the animal was allowed to continue until it licked the correct spout. At the start of each trial block, a single 3uL reward was dispensed at the now-rewarded spout. Criterion for passing *Shaping-1* was 500 μL consumed.

Shaping-2

Shaping-2 differed from *Shaping-1* in that trials were randomized between sides rather than blocked. Criterion here, and for all remaining sessions up to SEDS, was reaching 80% correct within a 30-trial moving window, and simultaneously performing above 50% on both left and right trials, at any point within the session.

Direction bias correction

To counteract animals' tendency to sporadically exhibit stereotyped direction bias, left/right stimulus probability was dynamically computed as a function of the animal's concurrent direction bias coefficient. A 10-trial moving window was populated with a [-1] for each incorrect left response, a [1] for each incorrect right response, and a [0] for each correct response. For each trial, the coefficient was the mean over the 10 previous trials. A coefficient absolute value between 0 and 0.25 resulted in 50% left-right stimulus probability; an absolute value between 0.25 and 0.75 resulted in a 33% chance of a stimulus toward the direction of bias; an absolute value between 0.75 and 1 resulted in a 17% chance of a stimulus toward the direction of bias. Trial runs with lick bias coefficients greater than 0.75 were therefore excluded from analysis.

Training on discrimination/shifting tasks

Stimuli

Of the 21 mice included in the imaging experiment, 14 underwent initial training with whisker stimuli, and 7 underwent initial training with odor stimuli. Subsequent comparison of stimulus encoding did not indicate any discernible differences between these two groups following the extradimensional set-shift. It should be noted that the hearing range of mice is 1-80kHz (Turner et al., 2005), which falls outside the range of the stimuli used to vibrate the whiskers.

For animals undergoing SD with whisker stimuli, stimuli consisted of a 35Hz sinusoidal stimulus and a 155Hz sinusoidal stimulus. The 35Hz and 155Hz stimuli were delivered bilaterally. These stimuli were generated by a pair of miniature base-frequency audio speakers (2'' diameter) coupled to a pair of plastic funnels which served to condense the sound waves into a 5mm diameter compression wave (75 dB). These stimuli produced oscillatory deflections of a majority of whiskers on the order of 10°, and active whisking was routinely observed during these epochs.

Odor stimuli consisted of murine-appetitive oil extracts. For the 7 mice undergoing initial training with odor stimuli, these stimuli were olive oil and sesame oil. The odor port was positioned 5mm below the animal's nostrils, with the airflow directed up toward the nostrils. Air was delivered through this port at a rate of 2.5 l per minute through 1/32'' inner-diameter polytetrafluoroethylene tubing. Outside of the odor stimulus epochs, clean air was delivered continuously through the odor port. At the onset of the odor stimulus epoch, air was rerouted through chambers containing the oil extracts, so that clean air was completely displaced by air from the oil container within 30ms.

Each trial began with a 500ms audible white noise (2kHz-17kHz) to indicate the start of a trial. Immediately following this cue, a whisker and/or odor stimulus (depending on the task phase as outlined in the table in Figure 1 and descriptions below) were presented for 2.5sec. The animal was permitted to lick the water spouts freely during stimulus presentation, though these anticipatory licks did not terminate the stimulus or trigger reward. Following the 2.5sec stimulus delivery, there was a response window of up to 1.5sec during which a lick to either port would end the trial, trigger delivery of a 3 μL water droplet (on correct trials), and begin the inter-trial interval. As shown in Figure 1B, licking toward the ultimately chosen lick port began well before the termination of the stimulus, and 95% of responses came within the first 0.346ms of the response window, a latency that corresponded with the first frame of imaging following stimulus termination.

Simple Discrimination (SD)

For the 14 mice undergoing initial training with whisker stimuli, on each trial a bilateral whisker vibration stimulus (one of two possible patterns) was delivered. Through water reward-mediated reinforcement, mice learned to lick the left lick port in response to the 35Hz stimulus and the right lick port in response to the 155Hz stimulus. For the 7 mice undergoing initial training with odor stimuli, animals learned to lick left in response to an olive oil odorant and right in response to a sesame oil odorant. Sessions consisted of up to 350 trials, and sessions were terminated early if an animal failed to respond to ten consecutive trials. An animal was considered to have reached criterion for the SD phase if at any point during a session it reached 80% correct performance, and simultaneously $\geq$ 50% correct on both left and right trials, within a 30-trial moving window. The SD phase tests the animal's ability to learn a stimulus-reward contingency and discriminate between two stimuli from the same dimension (i.e., two odors or two whisker stimuli). When criterion was reached, the current session continued to its end (up to 350 trials), and the animal was moved on to the subsequent task phase on the following session.

Compound Discrimination (CD)

An irrelevant stimulus (odor stimulus for mice initially trained on whisker stimuli and vice versa) was added on each trial. Both relevant and irrelevant stimuli were randomly and independently chosen for each trial. The same criterion standard was used as with SD: 80% correct performance (and at least 50% on both right and left trials) within any 30-trial moving window.

Intradimensional Shift (IDS)

A new pair of relevant stimuli replaced the stimuli used for SD and CD, while the irrelevant stimuli remained unchanged. For animals initially trained on whisker stimuli, the new stimuli were a 210Hz sinusoid (lick-left) and a train of Poisson-distributed square-wave

clicks averaging 210Hz (lick-right). For animals initially trained on the odor rule, the new stimuli were almond oil (lick-left) and orange extract (lick-right). This phase tests the animal's ability to learn a new stimulus-reward contingency and discriminate between two new stimuli from the same task-relevant dimension. The criterion for passing IDS was the same as for SD and CD.

Reversal (Rev)

The same set of relevant and irrelevant stimuli were used as in IDS, but the left-right mapping was reversed. This phase requires the animal to suppress and replace a previously learned stimulus-response contingency. Criterion was the same as in SD, CD, and IDS.

Extradimensional Shift (EDS)

The same whisker and odor stimuli were used as in IDS and Rev, but the previously irrelevant modality now became the relevant modality and vice versa. Because relevant and irrelevant stimuli were randomly and independently chosen on each trial, 50% of trials were congruent and 50% were incongruent. This phase requires the animal to associate a new stimulus *category*, the previously irrelevant stimulus modality, with a left-right response mapping. Criterion was the same as in all preceding task phases.

Intradimensional Shift 2 (IDS2)

The stimuli in the newly relevant modality were replaced, while those in the newly irrelevant modality were unchanged. This phase serves to ensure that the animal has learned to associate left-right stimulus mappings with multiple exemplar sets in each modality, thereby establishing an abstract attentional set within the newly relevant modality. Criterion was the same as in all preceding task phases.

Serial Extradimensional Set-Shifting (SEDS)

For each SEDS session, the relevant stimulus modality was chosen randomly at the start of the session. Stimuli during these sessions were the same stimuli used in the IDS2 phase (whisker: 210Hz sinusoid, left, and Poisson click train, right; odor: almond oil, left, and orange extract, right). Upon reaching criterion (still 80% correct and 50% on both left and right in a 30-trial moving window), the modality rule was automatically switched. This phase tests the animal's ability to integrate trial feedback to flexibly switch between task rules. As with previous phases, relevant and irrelevant stimuli were randomly and independently generated on each trial. To maximize the number of set-shifts in each session, sessions continued until animals reached satiety (ten consecutive non-response trials) or consumed 1.1mL of water.

Fixed tissue processing and imaging

Animals were transcardially perfused with 4% paraformaldehyde and 1x PBS. Heads were removed and incubated with all tissues intact in 4% PFA at 6°C. Brains were dissected after 24 hours and fixed in 4% PFA for an additional 24 hours before being dehydrated in a 30% sucrose solution (24-72 hours, until submerged). Tissue was sectioned coronally (in 45 μm sections) at −20°C and submerged in PBS until mounting. (When not in the cryostat tissue was stored at 6°C). Samples were mounted on 25x75x1 mm slides (Cole Parmer or Fisher Superfrost) with Sigma brand, DAPI-infused Fluoroshield mounting medium. For the L5 versus L6 PFC-MDT dual labeling experiment, Fluoroshield without DAPI was used, to enable BFP visualization.

Imaging was carried out on the Leica DM 5500 B microscope with a Leica DFC360 FX fluorescent camera (7x magnification) and EL600 light source, using a 10x apochromat objective with an NA of 0.4. Images were taken in two channels - the red channel used a CY3 filter cube (excitation filter 545/40, dichroic mirror 565, emission filter 610/76) at a 90ms exposure. The blue channel was captured with a DAPI filter cube (excitation 360/40, dichroic 400, emission 470/40) at a 100ms exposure. Both channels were imaged with full laser power and no gain. To allow for comparison across brain regions, both within and across animals, these imaging parameters were held constant for images gathered for the rabies tracing and fluorescent axon tracing experiments.

Images were acquired using the Leica Acquisition System (LASX) (Version 3.6) navigator feature to capture each sample as a series of 1281.71 × 957.36 um (1392x 1040 px) tiles, which were stitched (with no overlap or blending) by the software during acquisition to produce the complete image.

Rabies tracing

Monosynaptic inputs to PFC-VMS and PFC-MDT projection neurons were labeled by using a cross-sectional three-virus approach. At 4 weeks prior to sacking, AAV encoding the TVA rabies B19 glycoprotein (pAAV-EF1a-FLEX-TVA/B19) was injected into PFC. Virus was infused using a 36 g beveled NanoFil needle (WPI) and a 10 μL Hamilton syringe. Infusions of 250nL were made at each of four sites within PFC: AP +1.75mm, ML −0.2mm and −0.5mm, DV −2.0mm and −1.5mm (brain surface). Virus was infused at a rate of 50nL/min. In the same surgery, retrogradely transported rAAV2-CAG-Cre was injected into MDT (AP −1.2mm, ML −0.35mm, DV −3.2mm) or VMS (AP +1.25mm, ML −1.25mm, DV −4.7mm) in a volume of 500nL.

Following the dual infusions, Vetbond tissue adhesive was applied to the craniotomy over the exposed dura, and the skin was sutured into place using 6-0 silk sutures. Three weeks later, a second infusion surgery was performed to infuse EnvA G-Deleted Rabies-mCherry in PFC. Using a Nanoject nanoliter injector and a borosilicate pulled glass micropipette, 50nL of virus was infused at either a cortically superficial (ML −0.3mm) or deep (ML −0.6mm) site (AP +1.75, DV −1.7). The animal was again sutured and allowed to recover 1 week before sacking.

Fluorescent axon tracing

Surgical preparation, craniotomy, and infusion procedures were the same as those for GCaMP and stGtACR2 projection labeling experiments. AAV1-CAG-DIO-tdTomato was infused in PFC at four sites: AP +1.75mm, ML −0.2mm and −0.5mm, DV −2.0mm

and −1.5mm, at a volume of 250nL per site and a rate of 50nL/min. rAAV2-CAG-Cre (500nL) was infused in MDT (AP −1.2mm, ML −0.35mm, DV −3.2mm) or VMS (AP +1.25mm, ML −1.25mm, DV −4.7mm) in a volume of 500nL. Animals were sutured and allowed to recover for four weeks before sacking.

Processing rabies and fluorescent axon images

Coronal slices were mounted and imaged from ∼AP +3mm to ∼AP −4mm, spanning the frontal pole of the neocortex to the ventral/caudal hippocampus and surrounding regions. Imaging was performed at 1 μm/pixel resolution and tiled using Leica software. Image cropping, alignment, de-warping, registration to the Allen Common Coordinate Framework (Wang et al., 2020), and annotation of cell locations was performed using custom MATLAB algorithms adapted in part from the cortex-lab/allenCCF package (Shamash et al., 2018). Histological images were mapped to corresponding atlas sections by annotating images with manual control points and generating piecewise regression image transformations (MATLAB *fitgeotrans*). Individual labeled neurons were then individually annotated in MATLAB and mapped onto atlas locations using the Allen CCF structure tree (data.cortexlab.net/allenCCF).

Electrophysiological Recordings

stGtACR2 Photoactivation

AAV1-hSyn-stGtACR2-FusionRed was infused in PFC (AP +1.75mm, ML −0.2mm / −0.5mm, DV −2.0mm / −1.5mm, 250nL/site). Animals were sutured and allowed to recover for 4 weeks. On the day of the recording session, they were anesthetized under isoflurane (2%) and transitioned to 0.5% isoflurane over a 20min monitoring period. The craniotomy from the earlier viral transfusion was widened to an area of ∼2mm x 2mm. A 32-channel silicon probe, coupled to a 200 μm-core, 0.6NA optical fiber (H6b-style optrode, Cambridge Neurotech) was lowered into the brain at a rate of ∼100 μm/min to a depth of 1.7mm ventral at the tip. Recording were gathered using an Intan analog-to-digital acquisition system. Spikes were sampled at 20KHz with a 1Hz high-pass filter and 60Hz notch filter, and recording channels were referenced against an alligator clip secured to the neck muscle. Raw voltage recordings were later bandpass filtered between 250Hz and 20KHz using MATLAB'd *bandpass* function, and multiunit spiking activity was thresholded at −0.1mV.

Measuring muscimol-induced silencing

Anesthesia was administered as described above in the photoactivation experiment. A larger (∼2mm ML x ∼3mm AP) craniotomy was opened over frontal cortex. The animal's head was raised in order to provide a flat (rather than sloped) cortical surface over frontal areas. A multielectrode array (Innovative Neurophysiology Inc.) was arrayed in two rows of 8, spaced at 150 μm between columns and rows. The rows were arranged along the AP axis, with the most anterior recording site at AP +2.0mm, DV −0.5mm. and the two rows at 0.3mm and 0.5mm left of the midline. Muscimol (1 μg/μL) was infused at a rate of 50nL/min, for a total of 0.25 μL, through a 36 g needle positioned in between the most anterior pair of electrodes and angled 10° toward the anterior. Spontaneous activity during and following infusion was recorded and processed with the same settings as in the photoactivation experiment described above.

QUANTIFICATION AND STATISTICAL ANALYSIS

Tensor component analysis (TCA)

To estimate latent population activity associated with each task variable on a trial-to-trial basis, we used an unsupervised tensor component analysis (TCA) approach (Williams et al., 2018). Trial-aligned z-scored activity traces (trial x neuron x time) were first normalized to a nonnegative range and smoothed with a Gaussian kernel. They were then decomposed into a set of related trial, neuron, and temporal factors. We evaluated models using both standard TCA and nonnegative TCA, in which weights are constrained to positive values, ultimately selecting nonnegative TCA as it provided a more consistent fit. The trial components of these factors were then regressed onto the five primary task variables (whisker, odor, response, outcome, and rule) using MATLAB's glmfit function. Factors that were significantly modulated (Bonferroni corrected t test) by a given variable in the trial domain were then pooled to estimate temporal profiles for latent population activity underlying each task variable. Tensor reconstruction was performed by performing matrix multiplication on the component neuron*factor, trial*factor, and time*factor matrices. Temporal components shown in Figure 2G are from factors found to be associated with each task variable with a p value $< 10e^{10}$ using the GLM. This stringent criterion was used in order to include only the top 5% of most reliably modulated factors. Less stringent criteria resulted in the inclusion of factors with a high variance among temporal components.

To evaluate the intrinsic dimensionality of the data, decomposition ranks were compared across a range from 4 to 60; a maximal decomposition was also performed using a rank of R = N, where N was the number of neurons in each session, and used to benchmark the reconstruction error at lower ranks (Figure S8). The data were high-dimensional, with a high reconstruction error even with large rank values and without clear inflection points in the rank-error or rank-similarity functions (Figure S8B). To identify models that revealed task-related latent features, we also compared the accuracy of SVM decoders trained to classify features from trial components extracted with a range of rank values (Figure S8C), and found that classification accuracy increased with higher model ranks, approaching a plateau point around 35 factors. We compared the dynamics of the temporal components associated with feature prediction and found that, across a wide range of model ranks, the temporal profile presented in Figure 2G remains consistent (Figure S8D).

Please cite this article in press as: Spellman et al., Prefrontal deep projection neurons enable cognitive flexibility via persistent feedback monitoring, Cell (2021), https://doi.org/10.1016/j.cell.2021.03.047

Linear decoding with SVM classifiers

Population decoding was performed with maximum-margin linear decoders (MATLAB fitcsvm). At each iteration data were separated (bootstrapped) into equally sized training and testing sets, and in each set, trials were separated into equal numbers from each binary value for the feature of interest. To combine inputs from neurons across multiple sessions, and to remove inter-trial variability each of these trial groups was than randomly separated into 16 trial groups, each of which was averaged into one *super-trial* to serve as a decoder input (16 super-trials for one value of the feature of interest and 16 from the opposing value, for a total of 32 observations per model training). This number was calibrated to ensure robust trial subsampling within training and testing sets while removing sufficient trial variability to permit accurate decoding. Standard deviations for classification accuracy were obtained by iterating randomized training and testing over 500 subsamplings with replacement. Decoder testing performed on data from inter-trial intervals was run on binned activity values averaged over the 8 s post response epoch unless otherwise specified.

Principal components analysis (PCA)

PCA was used to identify the trial-aligned activity patterns responsible for the greatest variance within the activity space of the neural traces (Figure 5J). PCA was performed using MATLAB's native *pca* function, and the first three resulting components were plotted through trial-aligned time. PCA was performed separately on trial-averaged traces from PFC-VMS and PFC-MDT sets (neuron x time).

General Linear Model

MATLAB's *fitglm* function was used to fit a GLM model to projection cell type and topological location (depth from pial surface). Fitglm was also used to model multiple single neuron activity as a function of 7 task variables: whisker stimulus, odor stimulus, response direction (current trial), response direction (previous trial), trial outcome (current trial), trial outcome (previous trial), and task rule. Unless otherwise specified, GLMs were modeled with normal distributions, as linear functions (no interaction effects) with y-intercept terms, and with identity linkages. For analysis of individual neuron responses to task variables, a separate GLM was computed performed for each time point in the trial independently.

$$\hat{Y} = \beta_0 + \beta_1 p + \beta_2 d + \beta_3 p \cdot d$$

Euclidean distance and vector angles

Euclidean distance between pairs of trial averaged conditions was computed as the square root of the sum of the differences between the two conditions across all neurons in the set.

$$d_{xy} = \sqrt{\sum_{i=1}^{n} (x_i - y_i)^2}$$

Euclidean distance was also computed on activity vectors scaled by the vector weights of their corresponding SVM decoders in order to scale the amplitude of feature-selective cells relative to noise. Vector angles were computed as the dot product of the difference vectors, divided by the product of their norms. This value was converted into an angle of degrees by taking its inverse cosine.

$$\theta_{xy} = \cos^{-1}(x \cdot y) \div (\|x\| \cdot \|y\|)$$

Supplemental figures

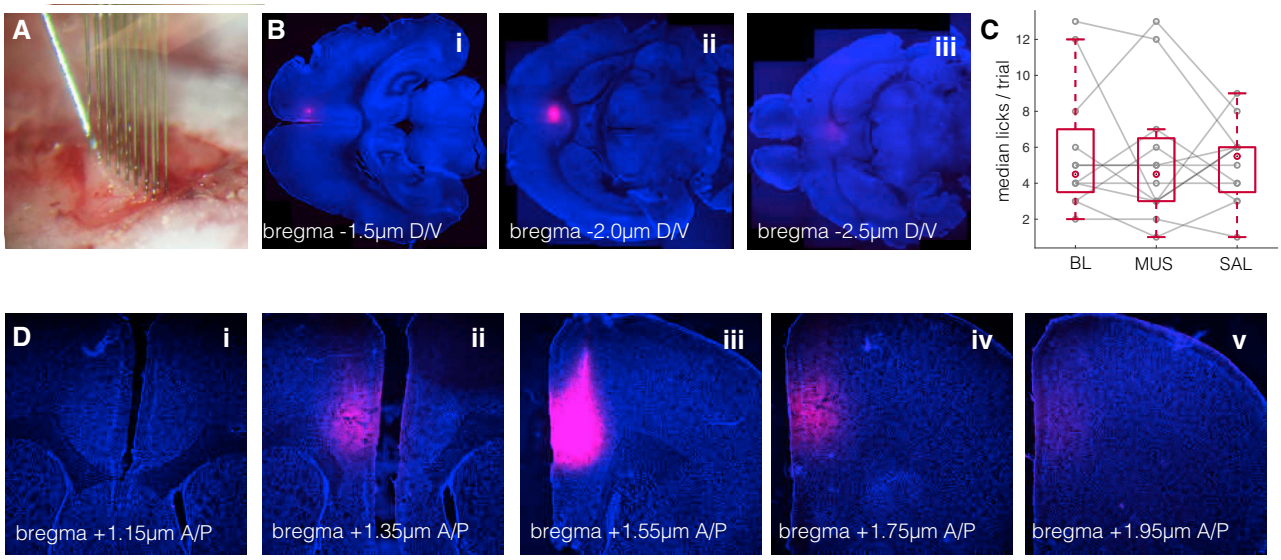

Figure S1. Muscimol infusion experiment, related to Figure 1

A. 16-channel multi-electrode array (Innovative Neurophysiology Inc.) used to measure the spatial extent of muscimol silencing effects. Photograph taken through a binocular surgical stereoscope (Kopf). The diagonal needle in the upper left is the infusion needle (36 g blunt, NanoFil), tilted to an anterior angle of 10° off vertical. The needle was positioned between the anterior-most pair of electrodes. Electrode rows were spaced at 150µm apart, 150µm spacing within rows.

B. Histological sections from a fluorescent muscimol injection at three horizontal planes. Red: Muscimol-TMR-X (Sigma Aldrich); Blue: DAPI.

C. Comparison of overt licking behavior in animals receiving muscimol, saline, and no injection. Rank sum for the BL-MUS comparison: $p = 0.88$.

D. Histological comparison from a fluorescent muscimol injection at five coronal planes. Red: Muscimol-TMR-X (Sigma Aldrich); Blue: DAPI.

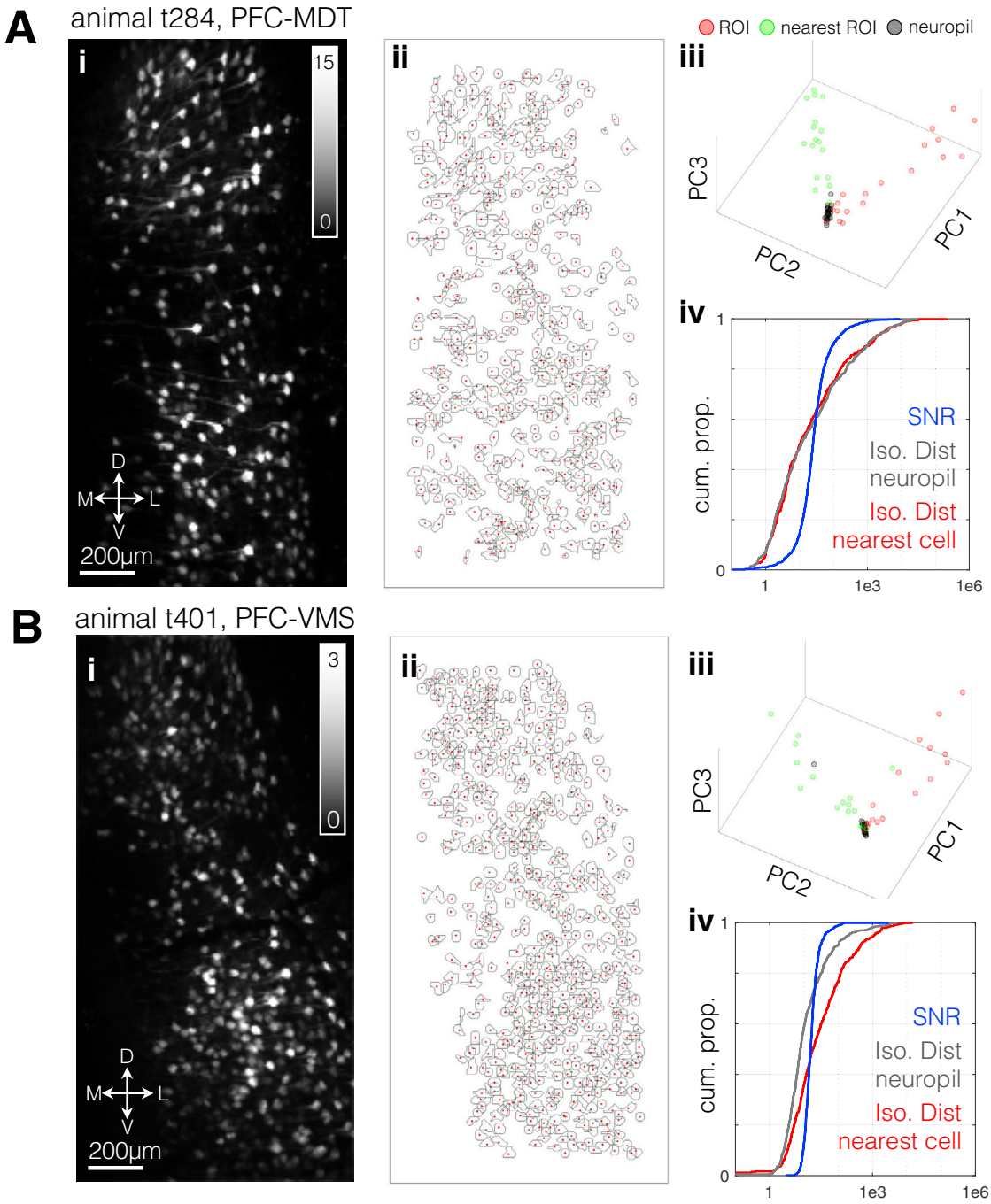

Figure S2. Example source localization with CNMF-E, PFC-MDT, related to Figure 2

A. Left: Session-wide activity projection for an animal labeled with GCaMP6f in PFC-MDT projection neurons. The value for each pixel corresponds with the pixel's standard deviation across all frames of imaging, normalized to its mean value (its session z-score). Center: Putative cell footprints extracted from the recording using CNMF-E. Grey contours are boundaries of spatial components, red dots are median centroids (N = 501 putative cells, 15437 frames, 0.289 f/s, galvano scanning). iii: First three PCA scores for each pixel in a represenative putative cell, its nearest neighbor, and neuropil, defined as an equal or greater number of pixels drawn from immediately outside the footprint and not within any other footprint. iv: Population cumulative distributions of isolation distances for the population. Red: isolation from nearest neighbor. Gray: isolation from neuropil. Blue: signal/noise ratios for pixels from identified neurons.

B. Same as (A), for a PFC-VMS animal.

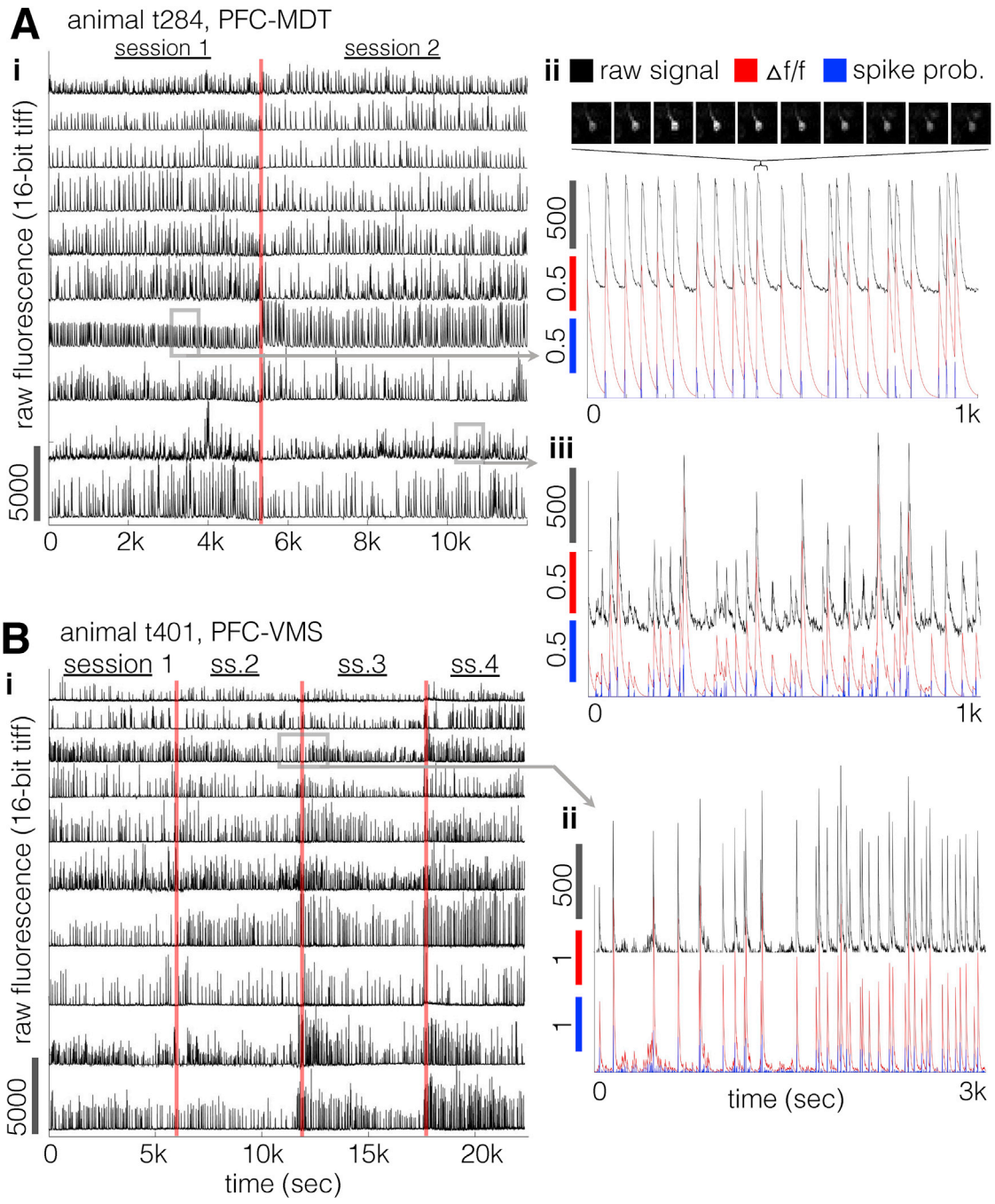

Figure S3. Example signal extraction, related to Figure 2

A. Example signals, PFC-MDT, same animal as (Figure S2A). **i**) Ten representative raw fluorescence traces from putative neurons identified in two successive SEDS sessions. **ii**) (top): Individual video frames from a single calcium transient event. Frames shown are downsampled to a rate of ½ the recording rate. Bottom: traces from the corresponding neuron as raw fluorescence (black, units are pixel brightness as unsigned 16-bit integers, maximum value 65,536), denoised ρf/f (red), and deconvolved instantaneous spike pobability (blue). **iii**) Example raw, denoised, and deconvolved traces for a second neuron.

B. As in (A), for a PFC-VMS animal (same as S2B).

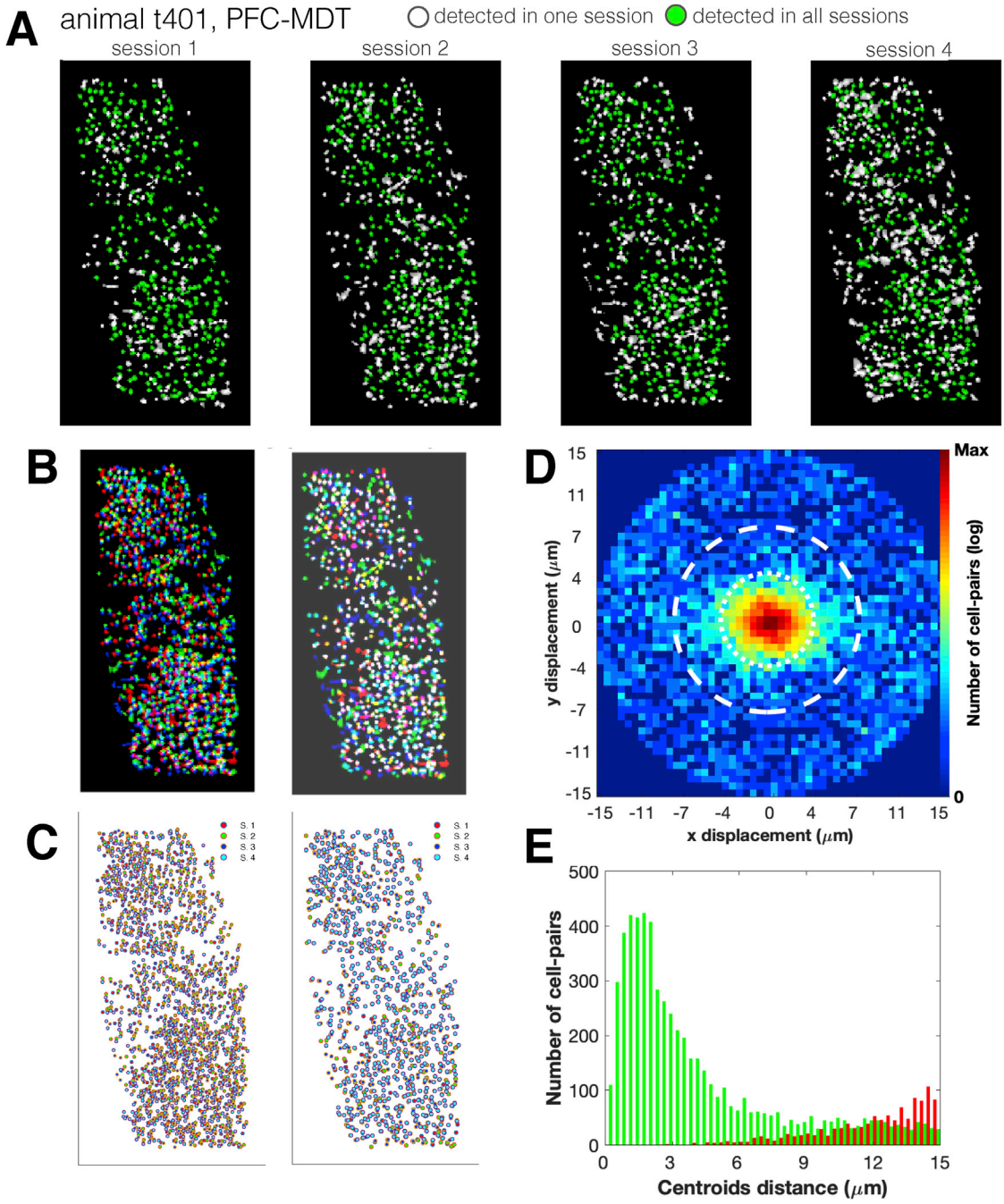

Figure S4. Example cross-session cell footprint alignment using the CellReg cell registration algorithm, related to Figure 2

A. CNMF-E-extracted cell footprints from four recording sessions, same animal as in S2B and S3B. Green-filled footprints are those detected across all recording sessions.

B. Pre-aligned (left) and post-aligned (right) cell footprints. Non-rigid alignment method.

C. Pre-aligned (left) and post-aligned (right) cell centroids.

D. Post-alignment offset of putative matching cell footprints.

E. Centroid distance histograms for putative matching (green) and non-matching (red) pairs of footprints.

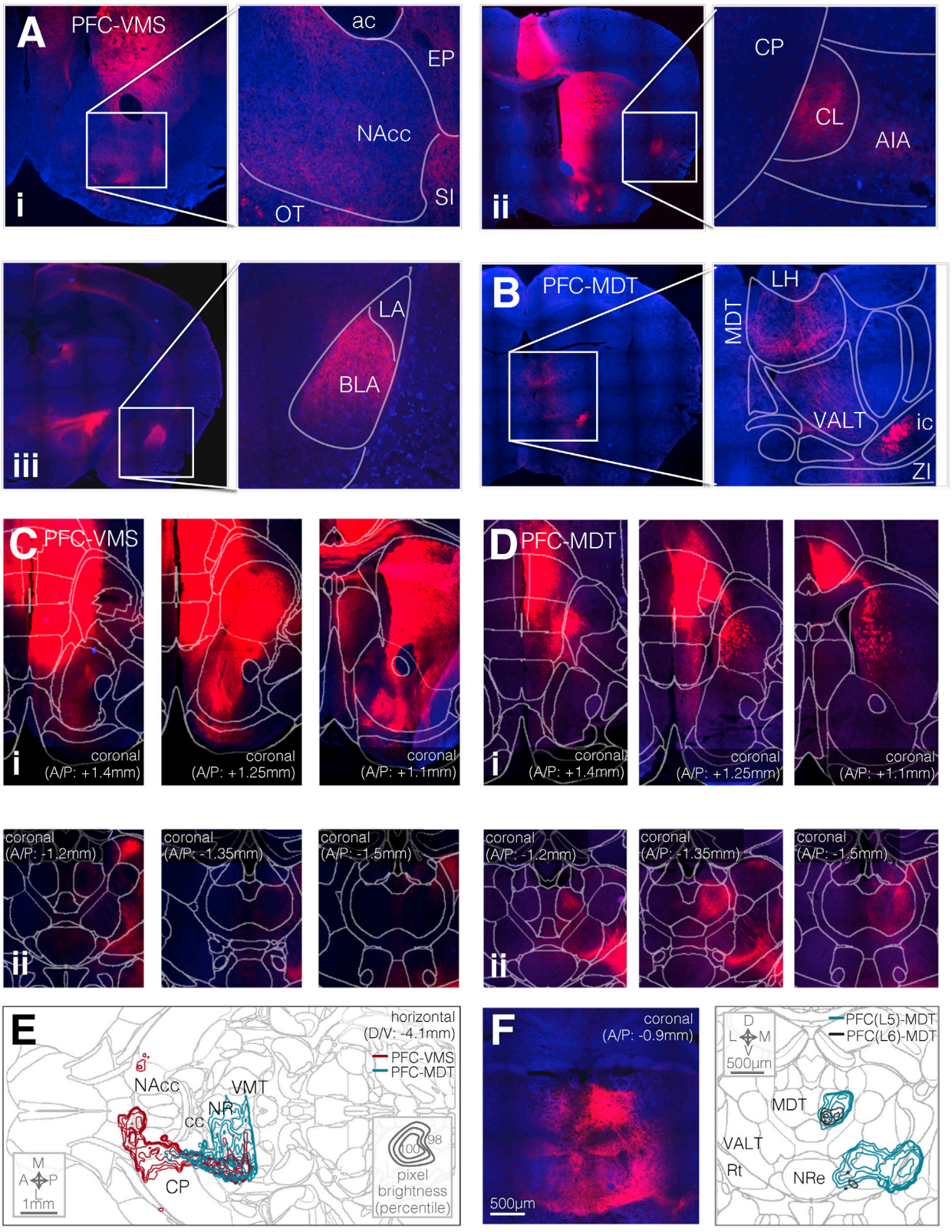

(legend on next page)

Figure S5. Fluorescence in long-range axons from PFC-VMS and PFC-MDT projection neurons, related to Figure 5

A. Long-range efferent axons from PFC-VMS neurons. Red: CAG-DIO-tdTomato; blue: DAPI. i) Fluorescent axons in the nucleus accumbens (NAcc), substantia innominata (SI), endopiriform nucleus (EP), and olfactory tubercle (OT). ii) Axon collaterals from PFC-VMS neurons in the claustrum (CL) and agranular insular cortex (AIA). iii) Axon collaterals from PFC-VMS neurons in basolateral amygdala (BLA).

B. Fluorescent axons from PFC-MDT neurons in mediodorsal thalamus (MDT), zona incerta (ZI), and the ventral anterolateral thalamic nucleus (VALT).

C. Coronal slices at multiple A/P cross-sections from within the same PFC-VMS labeled animal. i) Nucleus accumbens and surrounding regions at +1.4mm, +1.25mm, and +1.1mm relative to bregma (Allen CCF). ii) Medial thalamus and surrounding regions in the same animal, same laser and confocal microscope settings.

D. Coronal slices at multiple A/P cross-sections from within the same PFC-MDT labeled animal. i) NAcc and surrounding regions at +1.4mm, +1.25mm, and +1.1mm relative to bregma. ii). Medial thalamus and surrounding regions in the same animal.

E. Contour plots of axon fluorescence density from a composite of 5 PFC-VMS and 5 PFC-MDT labeled animals. Horizontal cross-section at 4.1mm ventral to bregma (Allen CCF). Concentric contours correspond with pixel brightness, which is represented as a percentile from each animal's pixel value distribution. Outermost of five concentric contours corresponds with the 98^{th} percentile, and the innermost enclosed contour corresponding with the 100^{th} percentile for pixel brightness.

F. Left: Example coronal cross-section of medial thalamus and surrounding regions from a PFC(L6)-MDT labeled animal (Cav-Cre in MDT and Flex-tdTomato in PFC). right: Composite contour plots for 5 PFC(L5)-MDT (green) and 2 PFC(L6)-MDT (black) labeled animals. Pixel brightness scale same as (E).

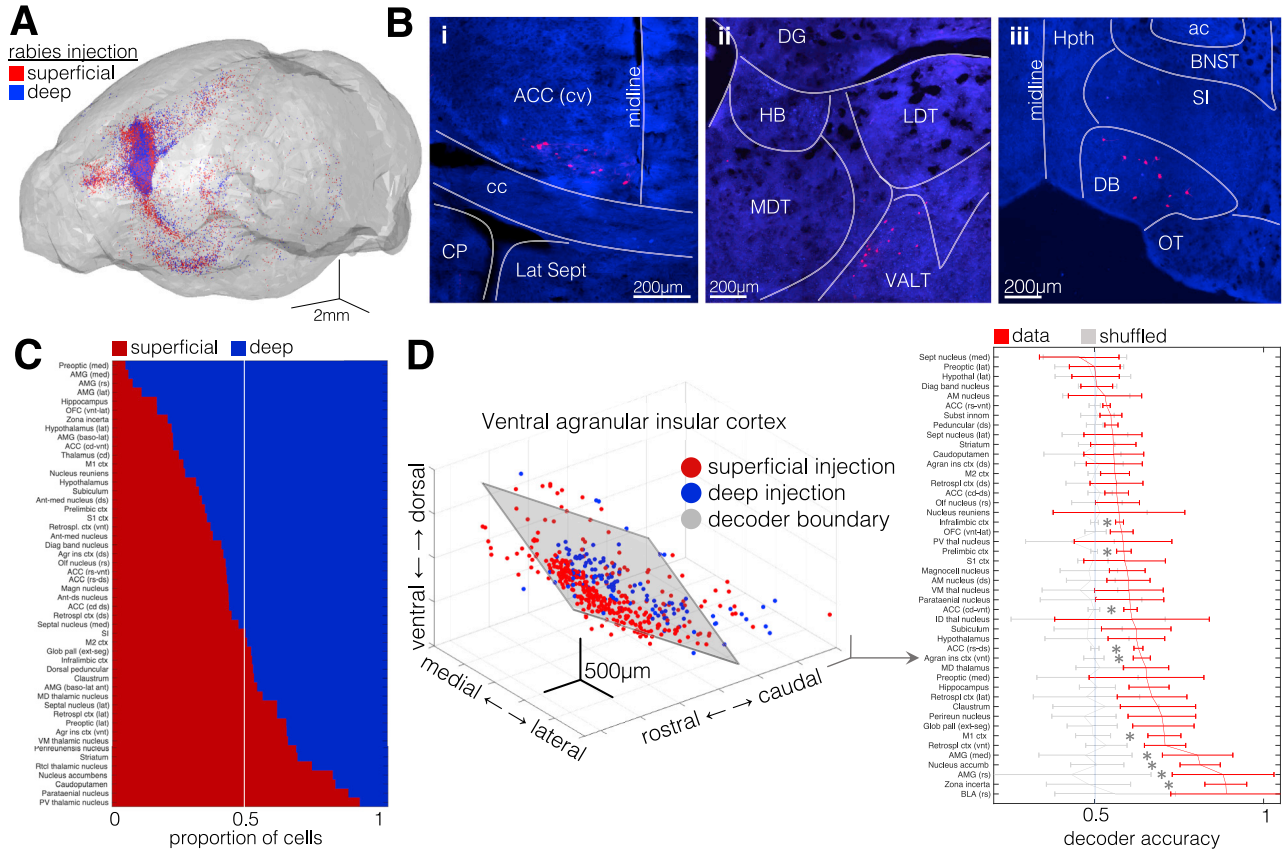

Figure S6. Rabies retrograde labeling experiment, related to Figure 7

A. Composite brain volume from the rabies tracing experiment. Shown is a three-dimensional rendering of the locations of starter cells in PFC labeled with EnvA G-deleted rabies-mCherry, as well as brain-wide retrogradely-labeled afferent cells synapsing onto deep and superficial projection populations (same animals, cells as Figures 7F–7H).

B. Example histological images of EnvA G-Deleted Rabies-mCherry labeling. i: labeing in caudo-ventral ACC. This region showed enhanced labeling in deep-injected animals relative to superficially-injected animals. ii: labeling in the ventral antero-lateral nucleus of the thalamus, one of numerous thalamic nuclei to show robust labeling, including medio-dorsal thalamus, retrospenial nucleus, paraventricular thalamus, nucleus of reuniens, and parataenial nucleus. iii: labeling in the diagonal band nucleus. Robust labeling was seen throughout the cholinergic nuclei of the basal forebrain, including the medial septum, the preoptic areas, and substantia innominata.

C. Relative cell densities in deep versus superficially-injected animals across brain areas. Regions shown are the 50 most cell-rich regions. **Abbreviations**: *ctx,* cortex; *med,* medial; *lat,* lateral; *cd,* caudal; *rs,* rostral; *ds,* dorsal; *vnt,* ventral; *AMG*, amygdala; *OFC*, orbitofrontal cortex; *M1*, primary motor; *Ant-med nucleus*, anteromedial nucleus; *S1*, primary somatosensory; *Retrospl.*, retrosplenial; *Diag band nucleus*, diagonal band nucleus; *Agr ins*, agranular insular; *Olf nucleus*, olfactory nucleus; *Magn. nucleus*, magnocellular nucleus; *SI,* substantia innominata; *M2*, secondary motor; *Glob pall (ext seg),* globus pallidus external segment. **Thalamic nuclei:** *MD*, mediodorsal; *VM*, ventromedial; *Rtcl*, reticular; *PV,* paraventricular.

D. Support-vector-machine-based decoders for within-region classification of cells from the two PFC injection depths. Abbreviations same as in (C). Inputs are the x,y,and z coordinates of each neuron, and each classifier was tested using 20-fold cross-validation and assuming uniform between-class distribution. Left: optimal support vector for ventral agranular insular cortex, which did not show a difference in total cell number between injection types, but in which a rostro-dorsal / caudo-ventral boundary between cell types is observed. Right: decoder performance, as well as performance on shuffled data, for each of the regions shown in C. Error bars: standard deviations. Asterisks: 2-sided t test, $p < 0.05$.

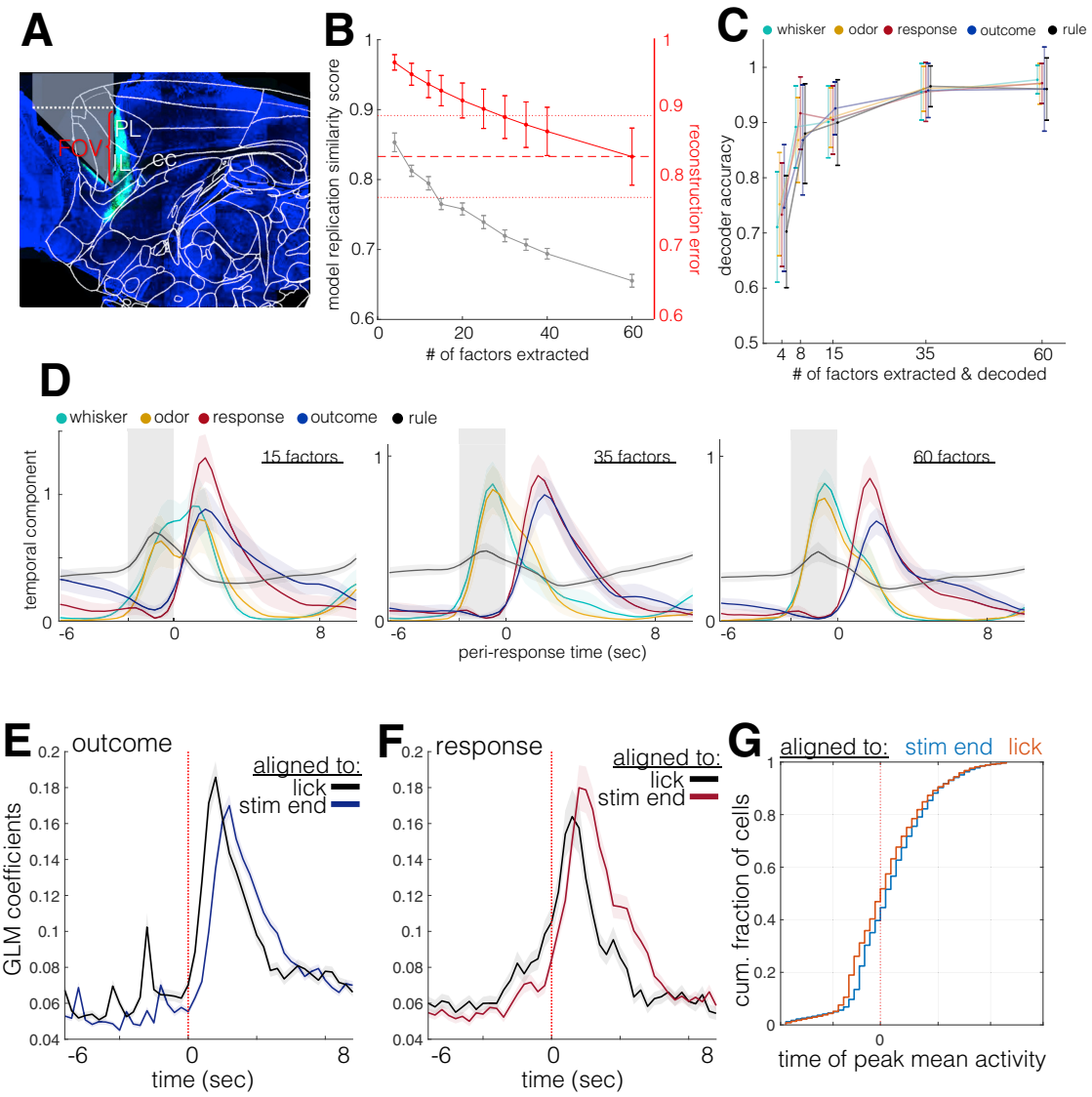

Figure S7. Temporal dynamics of response and outcome signals, related to Figures 2 and 3

A. hSyn-GCaMP6f or hSyn-DIO-GCaMP6f was injected at A/P +1.75mm, M/L −0.2mm and −0.5mm, D/V −2.0mm and −1.5mm. An atlas image from M/L −0.42mm was superimposed, with the corpus callosum (cc) used to co-register the atlas with the histological image. PL: prelimbic cortex; IL: infralimbic cortex; ACC(rd): rostro-dorsal anterior cingulate

B. Model similarity scores and reconstruction errors for a range of TCA rank decompositions. (Gray error plot): Mean ± SEM similarity scores across 21 animals for 5 replications of TCA decomposition, quantified as angles between latent factors across model replications. (Red error plot): reconstruction error for the same data and model rank selections. Dashed and dotted lines are mean ± SEM reconstruction error for the maximum rank used, which, in each animal's dataset, equaled the number of neurons.

C. Accuracy scores for SVM decoders trained to classify task variables using latent TCA factors as inputs. Same data as (A).

D. Mean ± SEM for temporal components corresponding with the factors most strongly modulated by each task variable, across a range of decomposition ranks.

E. Mean ± SEM for trial-aligned GLM coefficients of neurons significantly modulated by trial outcome direction. Modulated neurons include those with significance at any time point (Bonferroni-corrected for the 43 trial time points). Blue: coefficients aligned to stimulus offset; black: coefficients aligned to first lick within the response window.

F. Same as (A), for response direction. Red: coefficients aligned to stimulus offset; black: coefficients aligned to first lick within the response window.

G. Cumulative histogram of times of peak absolute activity (relative to the mean over the 43 trial time points) for each cell. Blue: peaks aligned to stimulus offset; red: peaks aligned to first lick within response window.

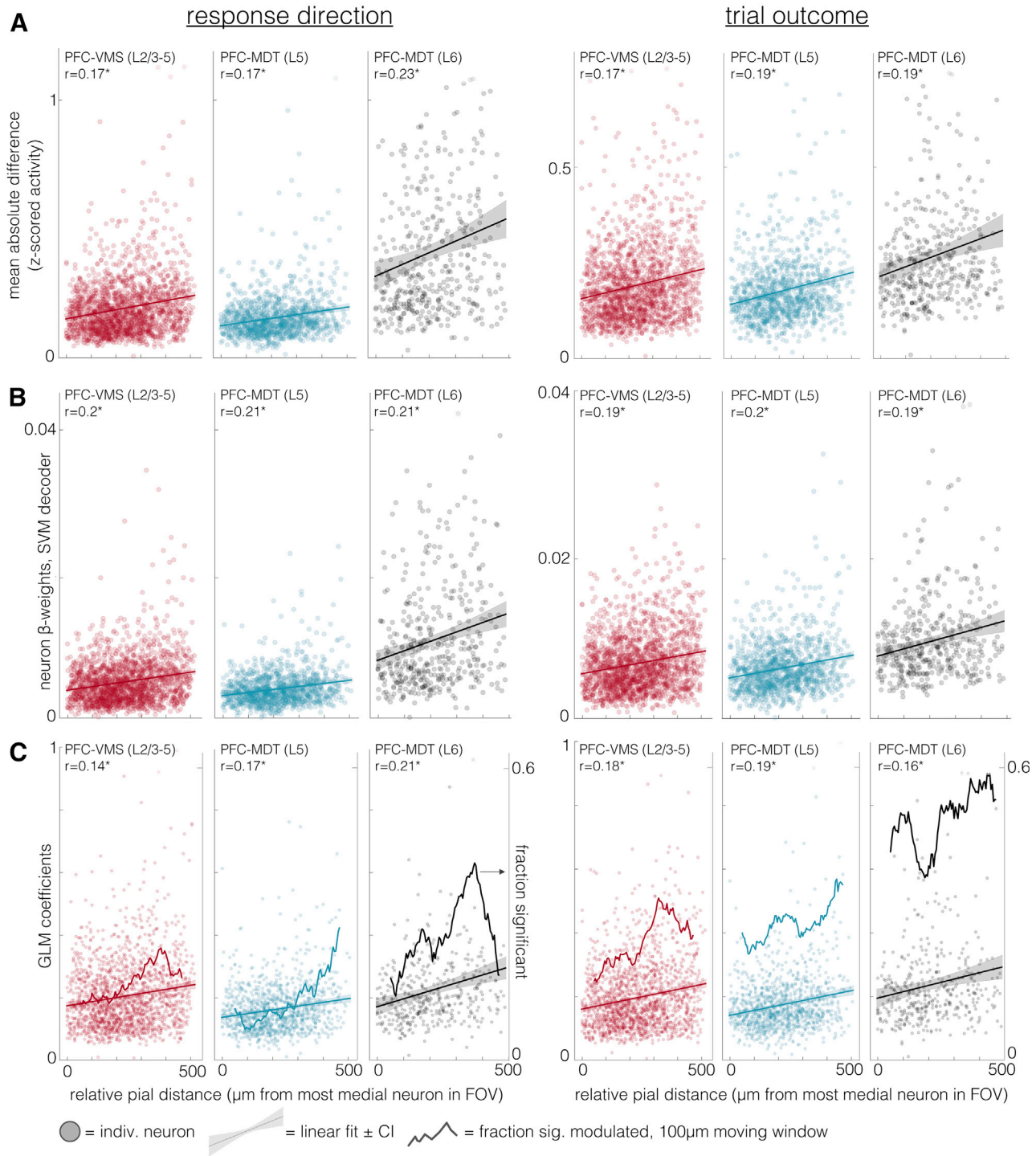

Figure S8. Modulation of trial feedback coding by laminar depth, comparison of statistical methods, related to Figure 7

A. Mean activity difference between conditions (respond left/right, trial outcome correct/incorrect), as a function of relative distance from the pial surface. Left: response direction; right: trial outcome. x axis: relative pial distance, defined as the distance from each neuron's centroid to the most medial/superficial neuron in each FOV; y axis: mean absolute difference in z-scored activity between conditions during inter-trial intervals. Mean difference by pial distance linear fit, response direction: PFC-VMS, $r = 0.17$, $p = 1.9 \times 10^{-13}$; PFC-MDT(L5), $r = 0.17$, $p = 6.6 \times 10^{-9}$, PFC-MDT(L6), $r = 0.23$, $p = 1.8 \times 10^{-6}$. Mean difference by pial distance linear fit, trial outcome: PFC-VMS, $r = 0.17$, $p = 1.4 \times 10^{-13}$; PFC-MDT(L5), $r = 0.19$, $p = 8.1 \times 10^{-11}$; PFC-MDT(L6), $r = 0.19$, $p = 8.3 \times 10^{-5}$. PFC-VMS N = 1770 neurons; PFC-MDT(L5) N = 1155 neurons; PFC-MDT(L6) N = 430 neurons.

(legend continued on next page)

B. Feature classification B-weights as a function of relative pial distance. x axis: as in (A); y axis: mean optimized B-weight for each neuron from 50 iterations of a SVM feature decoder that included all three projection subtypes in the same model, same neuron groups as (A). SVM B-weight by pial distance linear fit, response direction: PFC-VMS, r = 0.2, p = 1.5×10^{-17}; PFC-MDT(L5), r = 0.21, 7.7x10-^{13}; PFC-MDT(L6), r = 0.21, p = 8.3×10^{-6}. SVM B-weight by pial distance linear fit, trial outcome: PFC-VMS, r = 0.19, p = 1.6×10^{-15}; PFC-MDT(L5), r = 0.2, p = 1.4×10^{-11}; PFC-MDT(L6), r = 0.19, p = 6.2×10^{-5}.

C. GLM coefficients for response and outcome for each neuron as a function of relative pial distance. Solid trace corresponds with right y axis and equals the fraction of neurons significantly modulated by response/outcome withing a 100um sliding window of pial distance. GLM coefficient by pial distance linear fit, response direction: PFC-VMS, r = 0.14, p = 9.1×10^{-9}; PFC-MDT(L5), r = 0.17, p = 2.3×10^{-9}; PFC-MDT(L6), r = 0.21, p = 1.7×10^{-5}. GLM coefficient by pial distance linear fit, trial outcome: PFC-VMS, r = 0.18, p = 1.1×10^{-13}; PFC-MDT(L5), r = 0.19, p = 1.0×10^{-10}; PFC-MDT(L6), r = 0.16, p = 0.001.